TECHNISCHE UNIVERSITÄT
BERGAKADEMIE FREIBERG
Die Ressourcenuniversität Seit 1765

Microseismic event location and passive seismic imaging of crustal structures

Von der Fakultät für Geowissenschaften, Geotechnik und Bergbau
der Technischen Universität Bergakademie Freiberg

genehmigte

Dissertation

zur Erlangung des Akademischen Grades

doctor rerum naturalium
(Dr. rer. nat.)

vorgelegt

von **MSc-Geophys. Hossein Hassani**
geboren am 16. September 1983 in Rafsanjan-Iran

Gutachter: Prof. Dr. Stefan Buske (TU Freiberg)

Prof. Dr. Michael Korn (Universität Leipzig)

Tag der Verleihung: 22.07.2019

Versicherung

Hiermit versichere ich, daß ich die vorliegende Arbeit ohne unzuläßige Hilfe Dritter und ohne Benutzung anderer als der angegebenen Hilfsmittel angefertigt habe; die aus fremden Quellen direkt oder indirekt übernommenen Gedanken sind als solche kenntlich gemacht. Die Hilfe eines Promotionsberaters habe ich nicht in Anspruch genommen. Weitere Personen haben von mir keine geldwerten Leistungen für Arbeiten erhalten, die nicht als solche kenntlich gemacht worden sind. Die Arbeit wurde bisher weder im Inland noch im Ausland in gleicher oder ähnlicher Form einer anderen Prüfungsbehörde vorgelegt.

5. April 2019 MSc-Geophys. Hossein Hassani

"Human beings are members of a whole,
In creation of one essence and soul.
If one member is afflicted with pain,
Other members uneasy will remain.
If you have no sympathy for human pain,
The name of human you cannot retain."

(Persian poem by Sa'adi Shirazi, 13th century)

to my parents…

Overview

This thesis consists of two chapters. In chapter A, microseismic events in the mining area Schlema-Alberoda in south-west Saxony (Germany) are located and investigated based on a seismic imaging approach. In chapter B, the located events are used as seismic sources and through a passive seismic imaging technique, some crustal structures in this area are imaged.

The Schlema-Alberoda uranium mine was in operation until the end of 1990, and since then the mine pits and openings are under a controlled flood. This mine is located in a fault zone (Gera-Jàchymov) and many large and small scale faults dip into the bed rocks. This area is seismologically active and many earthquakes occurred during the last centuries before the start of mining operation in 1946. The mine seismicity was monitored over the last decades, during the mining operations and also afterward during the flooding phase. Many seismic events (mostly microseismic) occurred in the area over this period of time. The local seismic network in Schlema-Alberoda is still monitoring the seismicity of the area.

The aim of monitoring and analyzing seismicity in mining areas is to forecast ground motions and possible subsidence damage, as well as scientific studies on induced seismicity. For instance, in Schlema-Alberoda up to 6 meters of subsidence occurred during the mining activities (Penzel and Wallner, 2004) and this phenomenon can also occur after the end of mining operations.

In mining seismicity investigations, the event location accuracy is of great importance because even moderate uncertainties in the results (e.g. to an extent of hundreds of meters) can crucially affect interpretations. Previously, different localization methods were applied to locate seismic events in Schlema-Alberoda (see Künzel, 2013). In the present study, in order to

investigate the nature of seismicity, as well as the long-term role of mining-induced and triggered seismicity, a migration-based localization algorithm is developed to locate the recorded microseismic events. These events occurred during the last years after the end of mining operations (flooding phase). The localization method can be described as propagating the recorded P-wave primary arrivals at different stations back in depth and time to determine the spatial coordinates of the hypocenter and origin time of the event. To assess the accuracy of the localization results, a homogeneous and a 3-D velocity model are used in the migration algorithm and some of the located events are compared to the previous localization results of the same events as determined by Wismut GmbH.

In 2012, a 3-D active reflection seismic survey was conducted in Schlema-Alberoda and the resulting seismic image indicated many details about the subsurface structures (Hloušek et al., 2015). In the current study, the located hypocenters are compared to the 3-D reflection seismic image to determine possible correlations between the seismicity and reflectivity of the crustal structures. The velocity model used in the localization procedure is identical to the one used in the 3-D active seismic survey so that a direct comparison between the spatial location of the reflectors and the located hypocentres is meaningful.

The localization results are also compared to the geological information of the area collected through the investigations during mining operation. Based on this information, the nature of current microseismicity in the area is inspected and the findings are compared to a previous study.

Imaging faults and fractures can provide useful information for investigating the seismicity in Schlema-Alberoda. Besides that, another point of interest for imaging crustal structures in this area is the possibility of exploiting geothermal energy. Based on the investigations and measurements in the area

(Korobko and Grebenkin, 1960), the rocks are expected to attain temperatures higher than 150 ^{o}C in a depth of ~5 km. Using existing faults and fractures as natural hydraulic paths and heat exchangers is very favorable for geothermal energy exploitation. But those structures must be precisely imaged in order to evaluate the feasibility of using them in a geothermal project.

Imaging crustal structures in Schlema-Alberoda is challenging because the subsurface consists of heterogeneous crystalline rocks and the structures are dipping at steep angles. Through the 3-D active seismic survey, Hloušek et al. (2015) attempted to image a major fault along with other structures. This fault is the Roter Kamm which can be potentially used for geothermal energy exploitation in Schlema-Alberoda. Even though many reflectors and structures are imaged in that survey, the extension of the Roter Kamm could not be properly imaged.

The use of natural seismic sources for imaging subsurface structures (passive seismic imaging) is an alternative technique to the conventional seismic imaging methods in which artificial seismic sources are used for generating body waves. In some cases, passive seismic methods are advantageous to active seismic methods and can result in a more detailed image of the crustal structures.

The microseismic events in Schlema-Alberoda which are located with high precision through the migration-based approach, are proper seismic sources for a passive seismic imaging survey. Moreover, the hypocenters are located in a favorable position with respect to the illumination angle of the dipping structures, thus very useful for imaging these structures. In this study, the located events are used to image local crustal structures in the area, with a focus on the Roter Kamm. The imaging procedure is performed by 3-D coherency migration and only P-wave secondary arrivals are used in this approach. The final image is then compared to the results of the

aforementioned active seismic survey in the area. The 3-D velocity model used in the passive imaging procedure is identical to the one used for locating the events and in the active 3-D seismic survey, thus the two images (passive and active) can be compared directly. This comparison is done in order to evaluate the results and functionality of the passive imaging approach.

Contents:

A. Application of Kirchhoff prestack depth migration for locating microseismic events

B. Imaging crustal structures using microseismic events

A. Application of Kirchhoff prestack depth migration for locating microseismic events

A-1 Introduction

Small magnitude seismic events, which can be detected and recorded only by a local seismic network are called "microseismic events" or "microearthquakes". These events occur frequently, but they are scarcely noticeable because of their very small magnitude. In geophysical literature, there is no explicit standard for the magnitude below which seismic events are categorized as microseismic events. Nevertheless, seismic events with a magnitude smaller than 1 in local magnitude scale (M_L) are called as microseismic events (or microearthquakes) in most seismological texts. Different natural or artificial processes may cause microseismic events. The most dominant natural cause of these events are small-scale tectonic movements occurring along fractures and faults.

Microseismic events stimulated by human activities are generally connected to changes in load, volume or pore pressure and consequently result in a disturbance in the mechanical state of the corresponding subsurface structures (McGarr et al., 2002). The term "stimulated seismic events" refers to either "induced" or "triggered" events where, respectively, the changes in stress due to human activities is comparable to, or much less than the natural shear stress within the subsurface (e.g. McGarr and Simpson, 1997; Gupta, 2002). Mining operations, fluid injections into subsurface, underground fluid

removal and filling artificial water reservoirs and dams are the most common activities which cause stimulated microseismic events.

Fluid injection, which is a common operation in geothermal fields and hydrocarbon reservoirs, is a well-known source of induced and triggered microseismicity. Monitoring this phenomenon is very important and useful for characterizing geothermic and hydrocarbon reservoirs and evaluating the progression of hydraulic fracturing (see Shapiro, 2008).

Another source of stimulated microseismicity is mining operations where mass removals and excavations disturb the mechanical balance of the forces loaded on subsurface structures. The resulting accumulated stress can be released along the preexisting faults or may create new fractures. In mining areas, using explosives is a common operation for removing rock masses and the explosions can also be recorded by a local seismic network. Nevertheless, it must be noted that explosions are not stimulated seismic events themselves, however they may trigger accumulated stress in local subsurface structures. Mine seismicity had been recognized as an important phenomenon by the end of 19th century. The first observatory for monitoring mine seismicity was established in 1908 and operated until the end of 1930s in the Ruhr coal basin in Bochum (Germany). Some examples of stimulated seismicity in mining areas are discussed by McGarr et al. (2002). Gibowicz and Kijko (1994) comprehensively discuss mine seismicity and the involved mechanisms.

Although seismicity in mining areas is usually restricted to microseismic events, or so called “mining tremors”, in some cases large triggered events can also occur as a consequence of mining operations (e.g. Fernandez and Van der Heever, 1984; Gibowicz, 1979). The largest seismic event in a mining area occurred in 1989 in the Werra mining region in Germany (former East

Germany) with the magnitude of m_b=5.5, which caused destruction on the surface as well as in a deep area of 6 km^2. This event was stimulated by rough short- and large-period pore pressure changes within the crustal structures (Knoll, 1990).

In this chapter some of the recorded microseismic events which occurred in an abandoned mining area are located and compared to the results of a recently obtained 3D reflection seismic image of the area in order to investigate the causes of microseismicity in the vicinity of the mine.

A-2 study area

The Schlema-Alberoda uranium mine located in Schneeberg (Saxony, Germany) was a large vein-type uranium deposit (figure A.1). In this area, the history of uranium mining dates back to the end of 18^{th} century when the main aim of mining operation was to extract silver and cobalt. At the time, uranium was a byproduct. As a large uranium mine, Schlema-Alberoda was in production under the SDAG (Sowjetisch-Deutsche Aktiengeselschaft) Wismut from 1946 to 1990. The total production over 45 years from this mine was about 80,000 tons of ore from a total excavated volume of $45x10^7$ m^3. The excavations caused large-area subsidence in most of the area above the mine, which at some points is more than 5.5 m (Hiller and Schuppan, 2008).

At the end phase of the mining operations in Schlema-Alberoda, the results of intensive and comprehensive investigations showed that the orebody has been almost fully excavated to a reasonable economic level (Hiller and Schuppan, 2008). Monitoring the seismicity of the mine started during mining activities. The mine was allowed to flood after the end of the mining operations and the seismic network installed over the mining area by Wismut

GmbH (formerly SDAG Wismut) still monitors seismic events in this region.

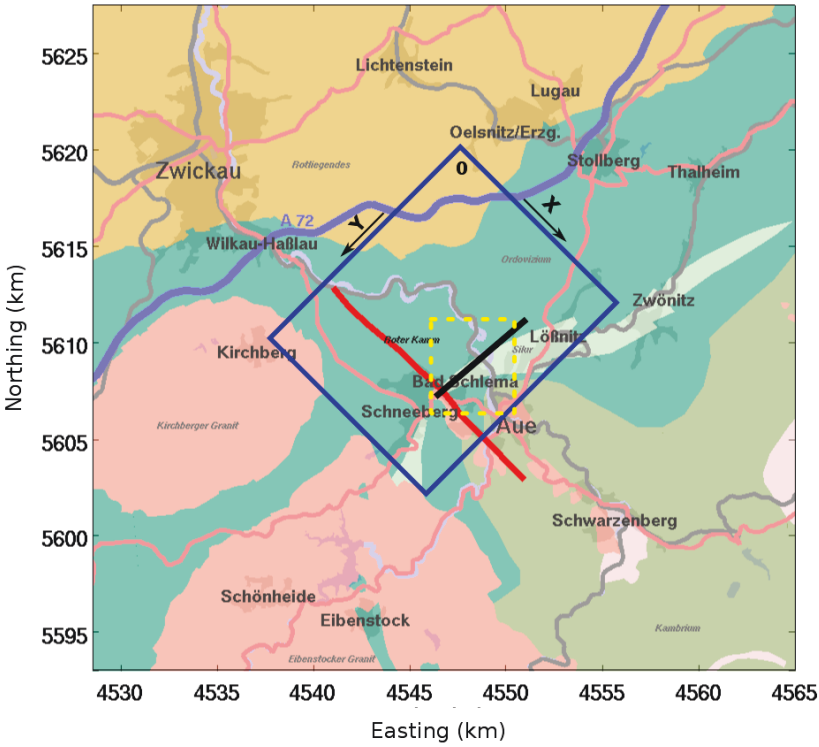

Figure A.1: Study area in Gauss-Krüger coordinate system. The blue solid box shows the local Cartesian coordinate system used in this study. The dashed yellow box refers to figure 3 (recording network). The solid black and red lines show the location of the profile shown in figure 2 and the surface extent of the Roter Kamm fault, respectively.

A-2-1 Geology

The geological properties of Schlema-Alberoda is described in detail by Hiller and Schuppan (2008). The surface elevation in the mining area is between 320 m and 520 m above sea level. This mine is a part of the ore complex Schneeberg-Schlema-Alberoda, positioned north-east of the Bohemian massif. The area itself is located at the nearly perpendicular intersection of two major tectonic structures, the Lössnitz-Zwönitz syncline and the Gera-Jàchymov fault zone with NE-SW and NW-SE extension respectively. One of the most important tectonic elements in this area is the Roter Kamm fault (figures A.1 and 2). The Roter Kamm is a vein structure located north-east of the Schlema-Alberoda uranium deposit, separating it from the Schneeberg bismuth-cobalt-silver-uranium deposit. The fault plane has a 50-70^{o} dipping angle towards the north-east (figure A.2) and its vertical displacement varies from a maximum of 580 m to a minimum of less than 100 m at the north-western part of the fault.

The dominant geological features in this area are granitic plutons. Furthermore, the south-eastern part of the mine is formed by gneiss and crystalline schists. In north-east, the adjacent synclinorium is composed of phyllites and green schists which form long folding structures. The Ordovician-Silurian-Devonian rocks at the core of Lössnitz-Zwönitz syncline are folded into Ordovician schist wings. The top of the granite dips towards the north-east and it is covered by the Lössnitz-Zwönitz syncline at the central part of the investigation area. Figure A.2 shows a vertical geological profile of the area with the faults which were known and mapped during mining operations.

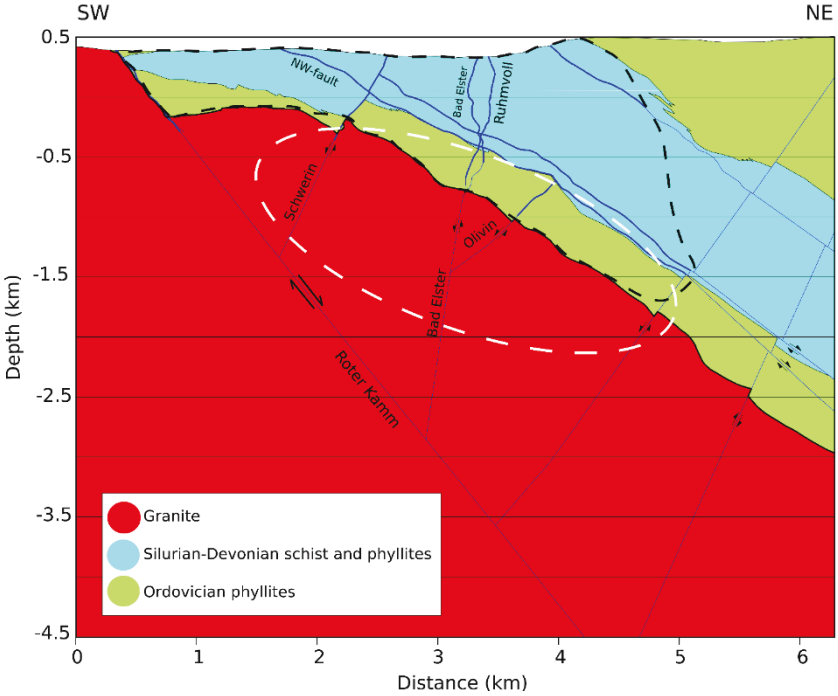

Figure A.2: A vertical geological section of the investigation area (Wallner et al., 2009). The location of this section is indicated by the solid black line in figure 1. The border of the mine is marked by the dashed line and the projected hypocenter area is shown by the white dashed ellipse. The thick blue lines represent the known part of the faults and the thin lines show the geological estimation of the fault plane extensions. For simplification, not all known faults are plotted in this figure. Mining took place along the uranium-rich ore body marked in blue which is a Silurian-Devonian complex of phyllites and schist.

A-2-2 Seismicity

Schneeberg is a seismologically active region and historic observations show that seismic events occurred in this area prior to the mining operation. Over 100 earthquakes are documented from sixteenth century until 1940s in Schneeberg with intensity levels between III and VI in MSK scale (Grünthal, 1988; Leydecker, 2007).

The documented earthquakes which occurred in the region prior to the mining activities and during the last centuries are focused in space and time. With the exception of some single events, most of them occurred in form of swarms. More than 50% of these earthquakes belong directly to the Gera-Jàchymov fault zone (Grünthal, 1988; Leydecker, 2007). Around half of the documented events in this region occurred between 1900 and 1908, though most of these events do not correlate spatially to local seismic events that occurred outside of this time period. Thus, the historic trend of the events does not show any distinctive feature of the seismicity in the area (Künzel, 2013) other than the possibility of stress release along the Gera-Jàchymov fault zone. Nevertheless, within the historical observations, no major seismic event was documented within the mine itself. A few events occurred between 1908 and 1913 in the south-eastern vicinity of the mine (Leydecker, 2007) indicating stress release in the area was already occurring before the start of the mining operation. However, any tectonic movement within the Gera-Jàchymov fault zone can affect the seismicity of the Schlema-Alberoda mining area (Künzel, 2013).

During the mining operations many seismic events also occurred within the Schlema-Alberoda mine. A relatively large magnitude event (M_L = 2.9) occurred in 1979 which caused deformations in mine pits and openings, as well as cracks and fissures in underground concrete supporting systems.

Geomechanical analysis showed that this event was the result of an inhomogeneous stress state within the granitic body as a consequence of intensive excavations and mass removal (Petschat, 1986; Hiller and Schuppan, 2008). After the end of the mining operations, while the mine allowed to flood from 1991, over 2000 seismic events have been recorded up until now by the local seismic network in Schlema-Alberoda with local magnitudes mostly less than 0.5.

The aforementioned studies provide a general overview about the history of natural and stimulated seismicity in the region, however precise seismic observations are a prerequisite for studying the causes of the current seismicity in more detail.

A-3 Earthquake location

The initial step in any earthquake investigation is to locate the hypocenter, e.g. the spatial coordinates of the point source from which the energy is released. One of the classical methods for earthquake location is the triangulation (circle) method which approximates the spatial coordinates of the hypocenter using P- and S-wave arrival times at 3 or more stations and the ratio between P- and S-wave velocities. Furthermore, the origin time of the event can be determined by a graphical method called "Wadati diagram" (Wadati, 1933) in which the P- and S-wave travel time differences are plotted versus P-wave arrival times at several stations.

Many methods for locating seismic events require the detection and picking of P- and S-wave travel times as well as the polarization of incident angles at each station. Roberts et al. (1989) show a method of locating earthquakes using recorded data from a 3-component single station based on the

polarization of the direct P-wave on vertical and horizontal components. In this method, an assumption of the S- and P-wave velocity is a prerequisite. Oye and Roth (2003) propose an automated location technique with focus on microseismic events with high main signal frequencies (150-400 Hz) based on analyzing particle motion on vertical and horizontal components.

A well-known and widely used time inversion method for locating local earthquakes is the Geiger method, which can locate the hypocenter and origin time of an event using only the P-wave arrival times at several stations and the P-wave velocity model of the area (Geiger, 1910). In this method, starting with an initial assumption of the hypocenter location and origin time of the event, P-wave travel times are calculated and compared to the observed travel times on the recorded seismograms. The initial assumed location and origin time are then corrected using the derivatives of arrival time function to reduce the differences between the calculated and observed arrival times (residuals). This procedure continues iteratively until the residuals are minimized.

In addition to the conventional earthquake location methods, seismic migration is an effective approach for locating seismic events. Migration-based location methods are especially effective and precise for locating microseismic events. Trojanowski and Eisner (2016) review and compare different location methods which detect and locate seismic events using full-waveform migration. Some migration-based earthquake location methods are mentioned in section A-6-1.

A-4 Data

A-4-1 Events and recording network

The data used in this study are seismograms of 135 microseismic events recorded by a local seismic network (operated by Wismut GmbH) between 1998 and 2012. The recording network consists of 56 stations, including 54 surface stations equipped with 4.5 Hz one-component (vertical) geophones and two borehole stations equipped with hydrophones. The digital recording sampling interval is one millisecond. The stations are densely distributed over the area above the Schlema-Alberoda uranium mine. The largest distance between two neighboring stations does not exceed 600 meters, making the network suitable to monitor local microseismicity (figure A.3). The events used in this study range in magnitude from -1.30 to 0.90 in moment magnitude scale (according to Wismut GmbH).

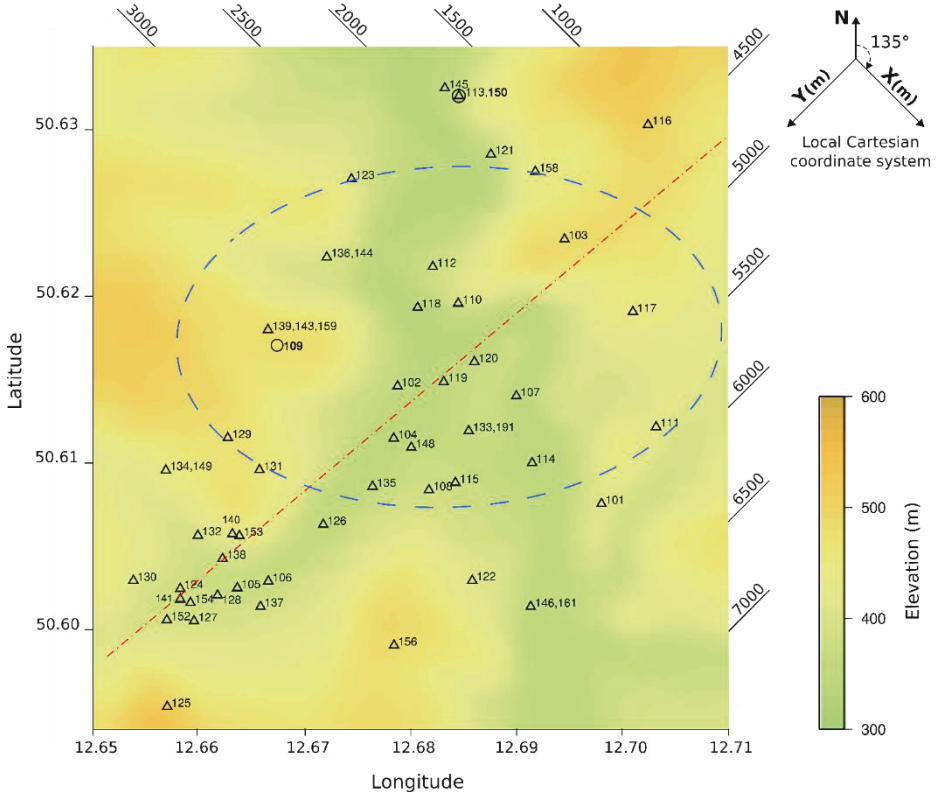

Figure A.3: Investigation area with seismic stations used to locate the events (after Hassani et al., 2018). The surface stations are marked by a triangle and the two borehole stations are indicated by a circle. The borehole stations 109 and 150 are situated at a depth of 527m and 645 m below sea level, respectively. The local Cartesian coordinate system (in meters) used in the location procedure is shown by diagonal lines. The area where the investigated events are located is shown by the dashed ellipse. The red dashed line refers to the position of the profile shown in figure 2.

A-4-2 Data preprocessing

For the event location method used in this study (section A-6), the accuracy of the P-wave arrival time picks is one of the key factors in the precision of the localization results. In order to maximize the picking accuracy, two filters are applied to reduce the noise level and sharpen P-wave first breaks. First, a band-pass 1-170 Hz Butterworth filter is applied to reduce the high frequency background noise and a notch filter at 50 Hz is used to eliminate electricity network noise. Also, those traces on which the P-wave arrival was not completely clear were eliminated to increase the precision of location procedure.

Figure A.4 shows an example of a raw trace and the applied filters. Errors in first breaks can happen as a result of filtering, such as a phase shift and ringing artifacts which may occur as a consequence of Butterworth bandpass filter. Therefore, to avoid possible errors in interpreting arrival times, the first breaks are picked from the filtered traces but always compared to the original waveforms. An example of vertical component waveforms recorded by a subset of 25 stations (23 surface and 2 borehole hydrophone stations) for a selected seismic event is shown in figure A.5. Due to the less attenuated high frequencies at depth, the traces recorded by the borehole hydrophones contain higher frequencies in comparison to those recorded by the surface geophones. The manually picked P-wave arrival times used for the location procedure are also shown.

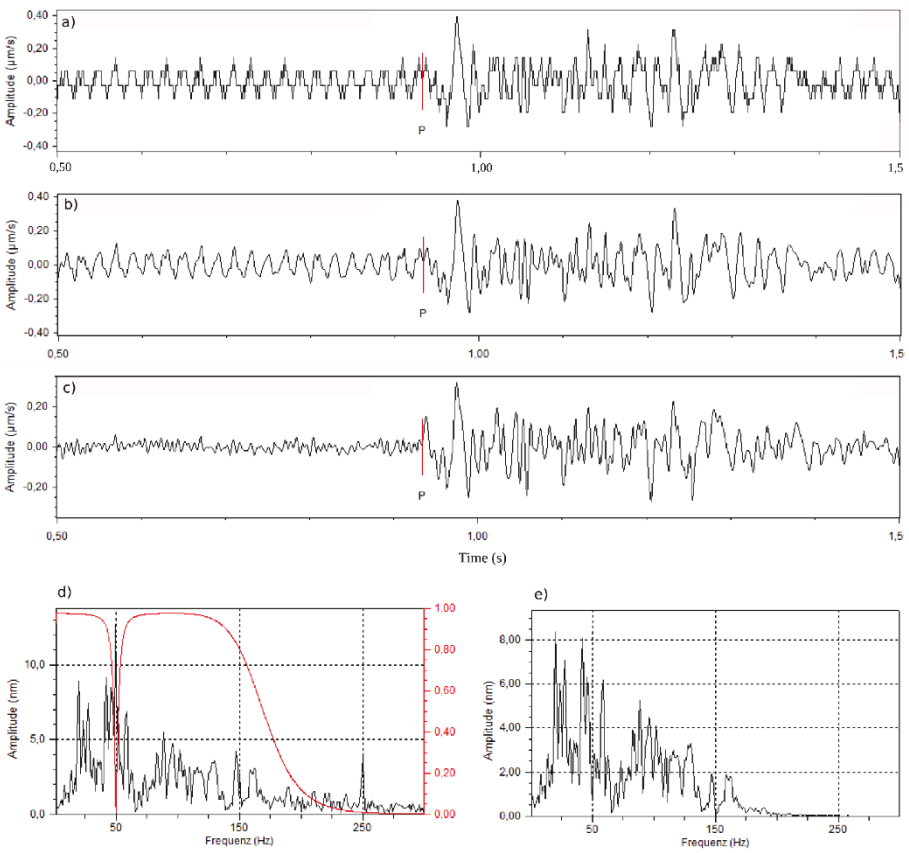

Figure A.4: An example of the applied filters; the recorded trace (a), after applying Butterworth bandpass filter (0-170 Hz) (b), after applying notch filter at 50 Hz (c), frequency spectrum of the unfiltered trace with the applied filters coefficient (the red curve) (d), frequency spectrum of the filtered trace (e).

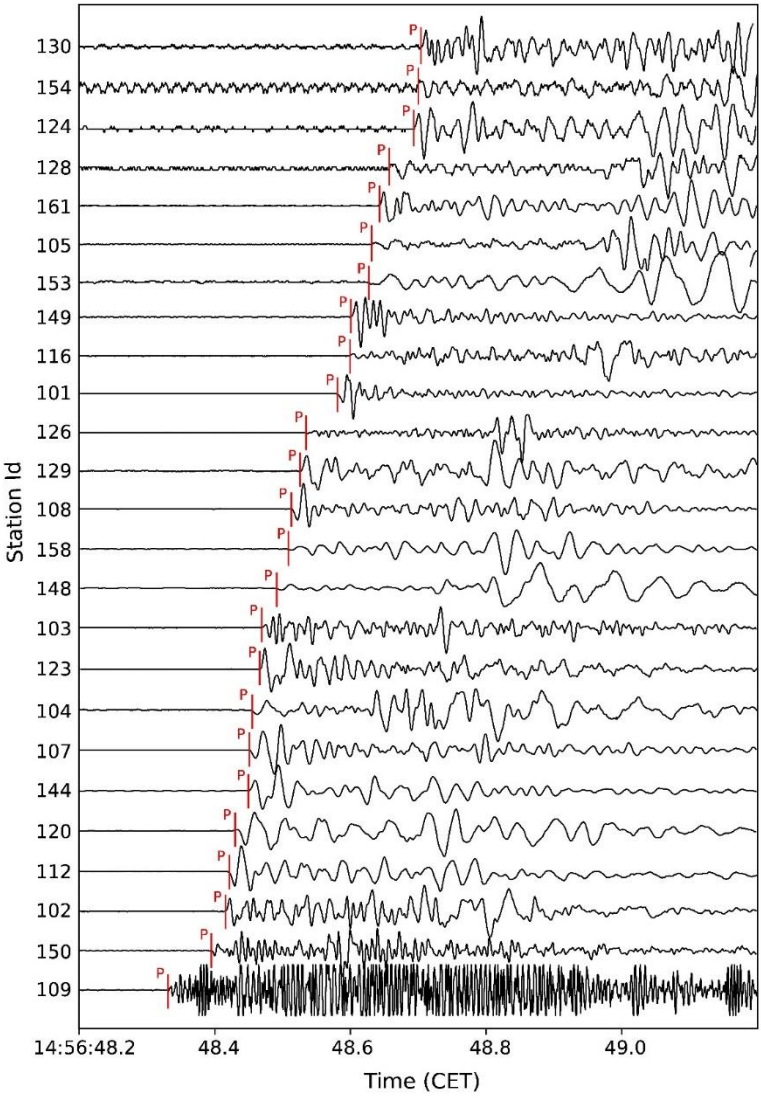

Figure A.5: Vertical component waveforms of a microseismic event recorded by 25 stations (after Hassani et al., 2018). Note that stations 109 and 150 are borehole hydrophones. The manually picked P-wave first arrivals are shown in red. The stations are ordered according to their distance to the hypocenter.

A-5 Seismic migration

A-5-1 Overview

In reflection seismic imaging, migration maps reflected phases to the correct position from where they are originated. In particular, migration suppresses diffractions and corrects the position errors and slope of dipping reflectors. Migration can be conducted in either the time or depth domain where the resulted image will be a time or depth section of the subsurface, respectively. Time migration is much faster and cost effective in comparison to depth migration, but in the case of large lateral velocity variations, time migration results in errors in the position and shape of reflectors in the final image. However, since depth migration is sensitive to the accuracy of the velocity model, if the velocity model is inaccurate, time migration can lead to a more reliable image than depth migration. Despite (generally) less accuracy, time migration is a very effective way to obtain an initial interpretation of the crustal structures.

In addition, migration can be performed before stacking the data (prestack migration) or after stacking the data (poststack migration). Stacking seismic data is a step in data processing which simulates a zero-offset section where sources and receivers are assumed to be at the same position (see Yilmaz, 2001). Poststack migration is performed on stacked data, i.e. zero-offset section, and is much faster than prestack migration, but it has some disadvantages. For instance, post stack migration results have a poor resolution in the case of dipping reflectors and it does not function correctly for diffractions.

The advantage of the chosen migration method depends on target structures, aim of the imaging procedure, demanded resolution and costs of the survey.

Time migration leaves diffractions (e.g. at the edges of reflectors) in a hyperbolic shape, therefore in the case of earthquake location, since the hypocenter is treated as a point diffractor, time migration is not an effective way of imaging.

Among various methods of migration, the focus in this study is on the Kirchhoff Prestack Depth Migration (KPSDM).

A-5-2 Kirchhoff Prestack Depth Migration

A fundamental technique in migrating seismic data is diffraction summation, which is based on Huygens principle of the superposition of a continuum of secondary point sources' zero-offset responses. This initial and simple technique belongs to the age of manual seismic imaging and does not account for the parameters which can affect the intensity of reflected amplitudes and the accuracy of the final image, especially when dealing with complex geological structures.

Kirchhoff migration is an improved version of the diffraction summation technique which considers spherical spreading of the wavefield, wavelet shaping factor and the directivity of the recorded wavefield at each receiver position by weighting the recorded amplitudes.

KPSDM is based on the Kirchhoff integral solution for the scalar wave equation (Schneider, 1978). In 3-D Cartesian space, consider a shot $S(x', y', z')$ with wavefield u recorded by receiver $r(x, y, z)$. The image value I for a subsurface point $m(x, y, z)$ is calculated by the weighted surface integration of the wavefield along diffraction surfaces:

$$I(m) = \frac{-1}{2\pi} \int_A \int w(m,r) \frac{\partial}{\partial t} u(r, t_s + t_r) dr \qquad [1]$$

In this equation, t_s and t_r are the travel times from the image point to the source and receiver respectively, and w is the weighting factor which takes the geometrical spreading and wavefield directivity at the receivers into account. The time derivative of the recorded wavefield ($\partial u/\partial t$) accounts for amplitude and phase corrections which (in 3-D migration) are proportional to frequency and a 90 degrees phase shift, respectively. The wavefield summation is conducted along the diffraction surface ($t_s + t_R$) which is called the "migration operator".

Following from equation [1], KPSDM is the summation of amplitudes over the records of source-receiver pairs. In a physical point of view, this can be described as smearing the amplitudes along the two-way traveltime (TWT) isochrones (wavefield back propagation).

The principle of the KPSDM is illustrated in figure A.6. The back propagated amplitude of each source-receiver pair is weighted with respect to the wavefield directivity (obliquity). Reflected wavefields are angle-dependent and most of the reflected energy from a point in depth will be recorded by receivers at near offsets to the depth point. Therefore, the recorded wavefield at the receivers with smaller offsets to the image point should have more contribution in constructing the image. Thus the recorded amplitudes are weighted proportional to the cosine of the wavefield incidence angle. For instance, comparing the wavefield recorded by receivers R4 and R7, the incidence angle of the ray coming from the diffraction point K is $\propto$ and β, respectively, where $\propto < \beta$. Therefore, the recorded reflection pulse at R4 gets a larger weighting factor during the migration and contributes more to the

image point at depth (note the thickness of the TWT isochrones in figure A.6). This discrimination is advantageous, especially when the primary P-wave reflections are used for imaging.

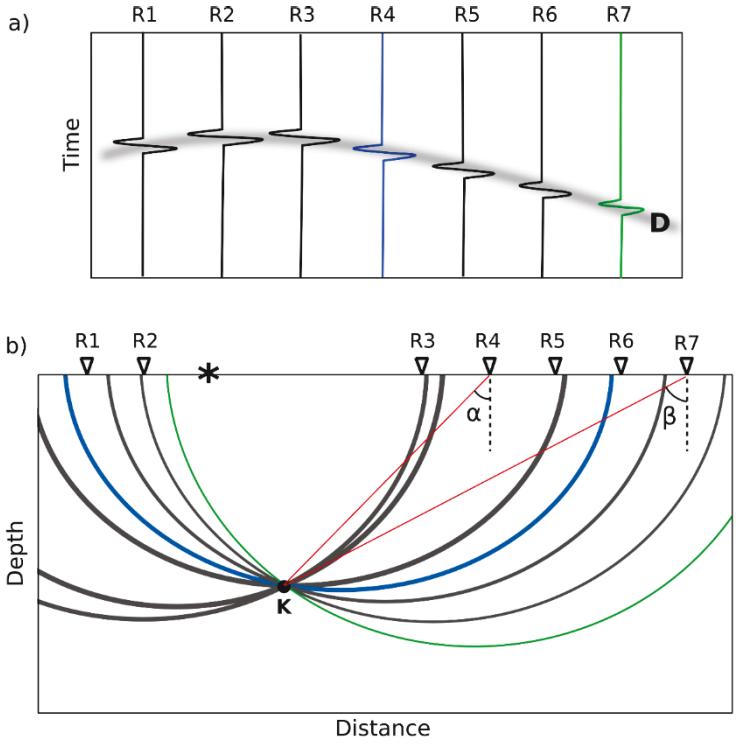

Figure A.6: Principle of KPSDM in 2-D. a) The reflected wavefield from the diffraction point K (in (b)) is recorded by the receivers. The integration operates over the diffraction curve D (migration operator). b) The recorded amplitudes are smeared into the depth over TWT isochrones and intersect at the position of the diffraction point K. The thickness of the TWT isochrones is proportional to the weighting factor. The asterisk shows the position of the source and the triangles are the receivers. The blue and green isochrones correspond to the receivers R4 and R7 respectively. For more details see text.

A-6 Locating microseismic events in the Schlema-Alberoda

A-6-1 Migration-based earthquake location

Besides classical earthquake location methods, various approaches based on seismic migration techniques, which are usually applied to reflection seismic data, have been implemented to locate seismic events. For example the use of reverse time migration is discussed by McMechan et al. (1985). Kao and Shan (2004) use absolute values of traces recorded at several stations to locate seismic events. In this method, traveltime calculations are based on the velocity of the phase with maximum amplitude (e.g. S-wave for local events). Through a so called "brightness function", the mean of the observed amplitudes (samples) at different stations is assigned to the corresponding point in depth at a specific time with respect to the velocity. A defined threshold of the overlap of the maximum amplitudes in depth determines whether a point is the source an event. The uncertainty in the spatial coordinates of the located hypocenter in this method may reach few kilometers.

Baker et al. (2005) show an application of Kirchhoff migration for locating earthquakes in the case of real time monitoring of local earthquakes, where the location process proceeds without explicit phase picking. In this method, the envelope of direct P-phase recorded by the vertical component of different stations is used in the migration procedure. The location algorithm is tested on a set of events with local magnitudes greater than 4.0 where the uncertainty in the hypocenters location was less than 10 km.

Rentsch et al. (2010) introduce a migration-based method for locating seismic events using multicomponent data. By analyzing P-wave polarization at different stations, this method propagates the energy recorded at stations

back in the depth based on ray tracing and a weighting factor inspired by Gaussian beams which restricts the back propagated energy around the raypath. This method is capable to locate seismic events with an accuracy in the range of tens of meters.

Grigoli et al. (2014) locate small magnitude local earthquakes ($M_L < 3.0$) by analyzing the coherency of the recorded P- and S-waves at 3-component stations. The coherency function is calculated based on short-term-average / long-term-average (STA/LTA) ratio of the P- and S-waves characteristic (energy) functions. A coherency value is then assigned to each point in depth and the maximum coherency indicates the location of hypocenter. The located events show an uncertainty (mostly) between 100 - 200 m and 30 – 50 ms in locations and origin times, respectively.

In an earthquake investigation, based on the aim of the study, the location method must be chosen with respect to the computation costs and the required precision of the results. On the other hand, the quality of the data (S/N ratio) and the recording network (one- or three-component) are determinant in choosing the appropriate method for locating seismic events.

In this study, a localization algorithm based on the 3-D Kirchhoff prestack depth migration (KPSDM) is implemented for locating microseismic events using only P-wave arrival times at one-component (vertical) receivers. Using this algorithm, the events can be located with high precision in the range of few tens of meters. In the localization procedure, the hypocenter is considered to be a point diffractor in the subsurface it is imaged by the KPSDM approach. Since the true origin time of the seismic event is unknown, the integration (see eq. [1]) must be performed for all possible origin times, resulting in a time-dependent image cube $I(y, y, z, t)$. Searching for the maximum image value within the image cube over time, determines the

hypocenter location and the origin time of the event.

A-6-2 Imaging pseudo synthetic data

Even though the observed waveforms have a high signal-to-noise ratio, they cannot be used as the direct input to the migration algorithm. Since the hypocenter location and time are determined from the image maximum, observed waveforms with consistent P-wave phase characteristics are ideal. As can be seen in Figure A.5, the observed waveforms have a clear P-wave onset, however the wavelet itself varies based on the station location and type, for example compare stations 109 (borehole), 144, 107 and 148. Furthermore, the first break indicates the moment where the source energy reaches the station. This time is independent of the wavelet characteristics and can be used as the energy arrival time. Therefore, the P-wave first breaks are picked from the observed seismograms and pseudo synthetic seismograms are created consisting of a normalized Gaussian curve (figure A.7) with its maximum at the corresponding picked time.

The Gaussian function is defined as:

$$f(t) = \frac{1}{\sqrt{2\pi\sigma^2}} e^{\frac{-(t-\mu)^2}{2\sigma^2}} \qquad [2]$$

where the picked P-wave arrival time is used as the mean of the distribution (μ) and the uncertainty of arrival time picking is applied as the standard deviation (σ). For this data set the recorded traces exhibit a very high signal to noise ratio with an uncertainty of about 3ms for the picked arrival times.

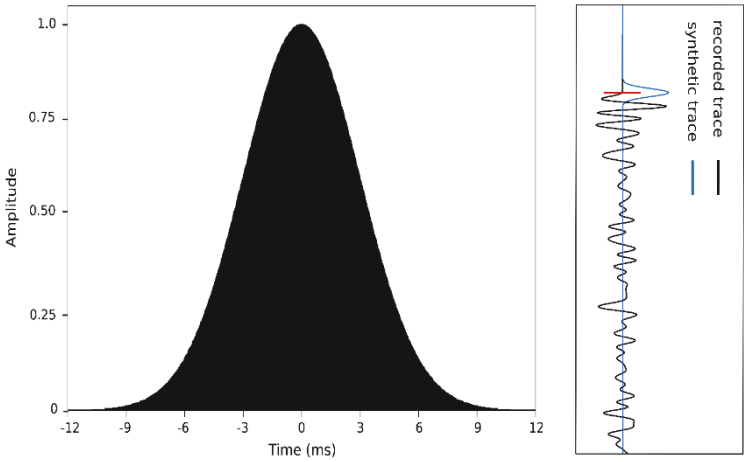

Figure A.7: Gaussian wavelet used to create pseudo synthetic seismograms for migration (left). The picked P-wave arrival time is the mean of the Gaussian distribution (here at time zero) with a 3 ms uncertainty. An example of a recorded trace, the picked P-wave first break (red spike) and the created synthetic trace (right).

In contrast with the application of KPSDM for imaging subsurface structures, the geometrical spreading and wavefield obliquity do not contribute to the localization algorithm since only the time of the first P-wave arrivals is considered and it is optimal to have the same contribution from different stations during the Kirchhoff integral computation. Thus the weighting factor $w(m,r)$ in equation [1] is set to 1.

The migration algorithm is implemented using a 3-D Cartesian grid with 25 meter spacing between grid points. The size of the 3-D cube is chosen to have a wide enough coverage over the investigation area (11.5 x 14.0 x 9.0 km) to include all possible hypocenter locations.

To ensure that the migration process covers all possible origin times, the data is iteratively migrated using 4 ms time steps over 2 seconds, starting from the latest P-wave arrival time and going backward in time. The 2 s time window accommodates all possible locations within the 3-D model grid. At each time step, the migration yields a 3-D image cube for the corresponding origin time. Figure A.8 shows a slice through the resulted images at different time steps.

After migration, the origin time and the spatial coordinate of the hypocenter is defined by searching for the maximum amplitude within all migrated 3-D cubes over time and space. An example with slices through the image cube for the resulting origin time is shown in figure A.9, where the maximum image value corresponds to the determined hypocenter.

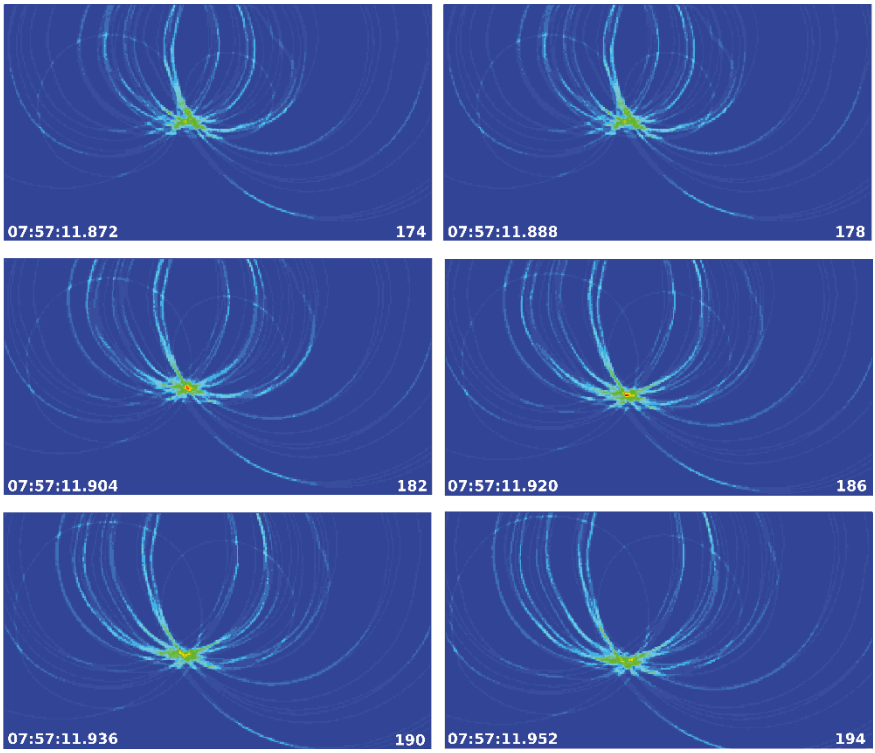

Figure A.8: A slice in y-z plane through the resulted images at different time steps. The actual time and the time step are shown at the bottom-left and -right of each slice respectively. To emphasize the visible difference in maximum amplitudes, the images are shown at 16 ms time difference (4 time steps). The amplitude reaches its maximum at the time step 186.

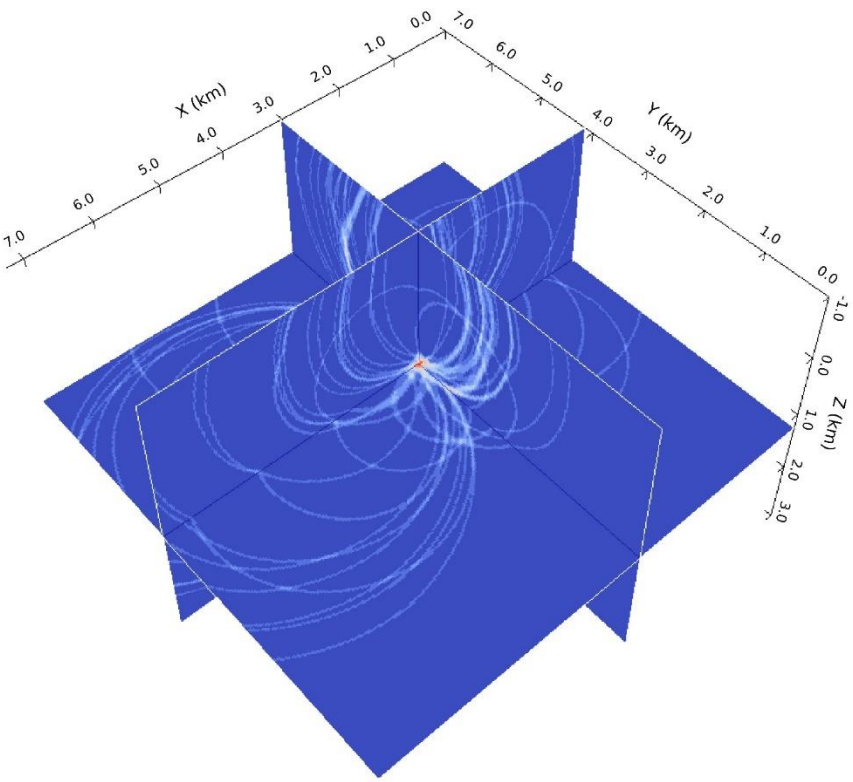

Figure A.9: Slices through the resulting 3-D image cube at the determined origin time. The maximum at the intersection of the slices corresponds to the hypocenter location (after Hassani et al., 2018).

A-6-3 Traveltimes calculation

According to equation [1], traveltimes from the image point to the source and receiver (t_s and t_r) must be calculated in order to compute the image value for

each image point. In the case of constant velocity, traveltimes can be calculated simply by the given spatial coordinates of the source and receiver. However, except for some cases where the velocity variations in the medium are negligible, one needs to calculate traveltimes with respect to the vertical and lateral gradients in velocity based on a reliable 3-D velocity model.

There are several approaches for calculating traveltimes in the case of spatially varying velocity $v(x, y, z)$, e.g. paraxial ray tracing (Červený et al., 1982), Gaussian beam ray tracing (Červený et al., 1984) and wavefront construction (Vinje et al., 1993). Another effective approach for calculating traveltimes is the use of the eikonal equation. In wave propagation problems, the eikonal equation is an approximation of the scalar wave equation where the traveltime of a ray is defined in relation to its spatial varying velocity:

$$\left(\frac{\partial T}{\partial x}\right)^2 + \left(\frac{\partial T}{\partial y}\right)^2 + \left(\frac{\partial T}{\partial z}\right)^2 = \frac{1}{v^2(x,y,z)} \qquad [3]$$

where in a medium with the varying velocity $v(x, y, z)$, the traveltime of the ray at the point $m(x, y, z)$ is $T(x, y, z)$.

The eikonal equation is a valid approximation to the scalar wave equation under one of these conditions: 1) The wave amplitude does not varying spatially. In the case of spatially inconstant amplitude, the traveltime function $T(x, y, z)$ is not a solution for the eikonal equation. 2) When the amplitude varies in space, the eikonal equation can be a reliable approximation to the scalar wave equation only if the wavelength is not much larger than the extent in which the velocity variation occurs (Officer, 1958). In practice, the eikonal equation can be considered as an approximation to the scalar wave equation when the velocity contrasts in the subsurface are

not very sharp (Yilmaz, 2001). This means that in largely contrasted velocity mediums, a direct calculation of the traveltimes from the eikonal equation does not yield accurate results.

Finite difference approximation of the eikonal equation can be used for calculation traveltimes in slightly varying velocity mediums (e.g. Vidale, 1988). Podvin and Lecomte (1991) propose a technique for calculating first arrivals traveltimes in mediums with sharp velocity contrasts, which is an extension of Vidale's method with respect to the concept of Huygens' principle and Fermat's minimum time principle. In this method, the 3-D medium is divided into small constant velocity cubes (figure A.10-a) with dimensions smaller than velocity anomalies extent. The traveltime of a grid point is calculated regarding to the traveltimes of the neighboring grid points, considering 3 different wave propagation modes; transmission, diffraction and refraction. After calculating all possible arrival times at a grid point, the minimum one is picked as the traveltime.

Referring to figure A.10-b, in the case of 3-D transmission, a wavefront can be transmitted through the interface MNPQ to the point R. Four different scenarios are applicable relating to each half of the interface through which the wavefront can be transmitted. For instance, the locally plane wavefront defined by the traveltimes of the points M, N and Q can reach point R if:

$$0 \leq (t_N - t_M) \leq (t_Q - t_N) \leq (h/v)^2$$

and

$$2(t_Q - t_N)^2 + (t_N - t_M)^2 \leq (h/v)^2$$

In this case, the arrival time at point R will be:

$$t_R = t_Q + \sqrt{(h/v)^2 - (t_Q - t_N)^2 - (t_N - t_M)^2} \qquad [4]$$

where t_M, t_N and t_Q are the traveltimes of the grid points M, N, Q respectively, v is the velocity within the current cube and h is the grid spacing. This calculation must be done for all 24 neighbouring interfaces to point R in the 3-D space (figure A10).

Diffracted waves can be originated from 8 corners and 24 edges in 3-D structure. Consider the cube in figure A.10-b:

$$t_R = t_M + (h/v)\sqrt{3} \qquad [5]$$

Equation [5] calculates the diffracted wave arrival time for a wave starting at point M and ending at point R. The arrival time of the diffracted wave from the edge MN at point R is calculated as:

if $0 \le (t_N - t_M) \le h/v\sqrt{3}$, then

$$t_R = t_N + \sqrt{2}\sqrt{(h/v)^2 - (t_N - t_M)^2} \qquad [6]$$

In the 3-D space, arrival time of the head waves (refractions) are calculated by computing 1-D transmissions and 2-D transmissions and diffractions at the boundary (edges and surfaces) between two adjacent cubes with different velocities. Suppose that $v' > v$ in figure A.10-b, a refracted wave from point Q arrives at point R (1-D transmission) where:

$$t_R = t_Q + h/v' \qquad [7]$$

A 2-D transmission occurs on the front plane of the cube with the contribution

of the edge QN (figure A. 10-b) where:

if $0 \leq (t_Q - t_N) \leq h/v'\sqrt{2}$, then:

$$t_R = t_Q + \sqrt{(h/v')^2 - (t_Q - t_N)^2} \qquad [8]$$

Also 2-D diffractions occur on interfaces in the 3-D model. For example, considering N as a point diffractor (figure A. 10-b), the arrival time at R will be:

$$t_R = t_N + (h/v')\sqrt{2} \qquad [9]$$

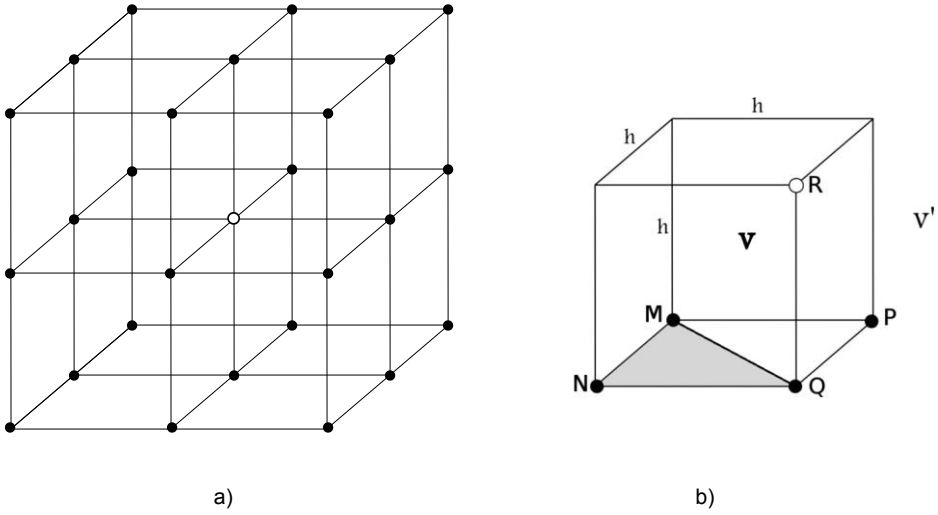

a) b)

Figure A.10: 3-D model used in Podvin and Lecomte (1991) method for calculating traveltimes. a) The medium is divided to constant velocity cubes where the traveltime of a grid point (the open circle) is calculated using the known traveltimes of neighboring grid points. b) A single cube with the velocity v surrounded by neighboring cubes with the velocity v'. For details, see the text.

In this study, the method of Podvin & Lecomte (1991) is used to calculate traveltimes for migration. It is applied using a 3-D velocity model of the area (figure A.11) developed through seismic tomography (Hloušek et al. 2015). Within the area of investigation, the 3-D velocity model is characterized by lateral velocity variations with a contrast of ~1000 m/s change in 300 m lateral distance. In the depth interval of ~700 – 1700m in which the events are expected to be located (based on the information from previous studies), the velocity range between 5000 and 6000 m/s. In deeper parts of the model the velocity variation is less. This 3D velocity model is derived from a 3-D wide angle seismic survey and its validity has been evaluated by comparing the calculated and observed first arrival travel times (Hloušek et al. 2015).

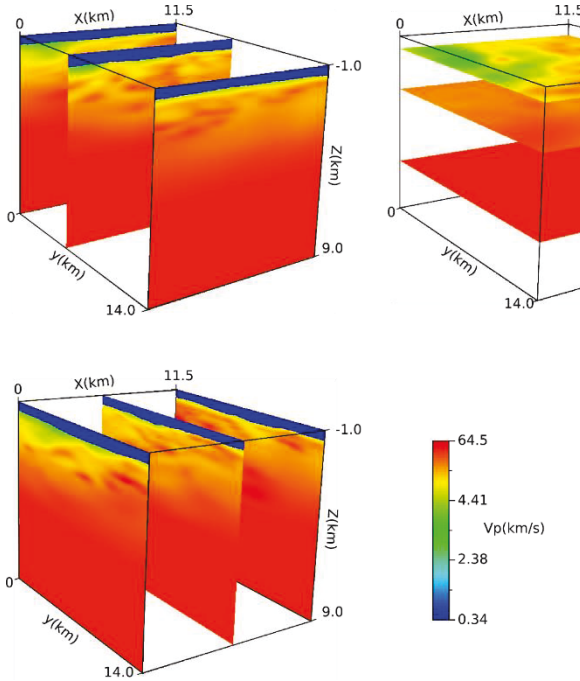

Figure A.11: The velocity model used for calculating traveltimes (developed by Hloušek et al. 2015).

A-6-4 Localization results

The located hypocenters are plotted in figure A.12. The obvious extent of the hypocenters is diagonal in x-y plane in the locally defined Cartesian coordinate system (west-east in latitude-longitude coordinate system, see figure A.3). This trend correlates to the extension of the excavated area of the mine (figures A.2 and A.15). Also, in the y-z plane, a clear cluster of the hypocenters can be seen dipping in the negative y direction, which is towards north-east, the same as the dip direction of top of granite (figure A.2). The coordinates and origin times of the located events are given in the appendix. More details about the characteristics of the hypocenters scattering pattern is discussed in section A-6-6.

It is important to consider the potential sources of error and uncertainty in the hypocenter locations. The initial source of error stems from the manually picked arrival times. With respect to the careful pickings and considering the sampling frequency and data quality, the error in arrival times is defined as 3 ms. As discussed in section A-6-2, to account for this uncertainty, this error is applied in the Gaussian pulse (equation [2]) used in pseudo synthetic seismograms. The second uncertainty stems from the time step used in the iterative migration. A fine sampling with an iteration every 4 ms is used for the migration, however even this fine sampling can introduce error in the location results. The third source of error is the resolution of the 3-D model grid (25 m grid point spacing) which also affects the accuracy of the final results. The other uncertainty which can affect the location results is the possible small errors in the 3-D velocity model. The accuracy checks on the velocity model (see section A-6-3) are convincing and small possible errors are not included. For an average velocity of 5700 m/s, the total spatial error in hypocenter location due to the aforementioned uncertainties is ~50 m which is minor and does not significantly impact the calculated locations and

further interpretations.

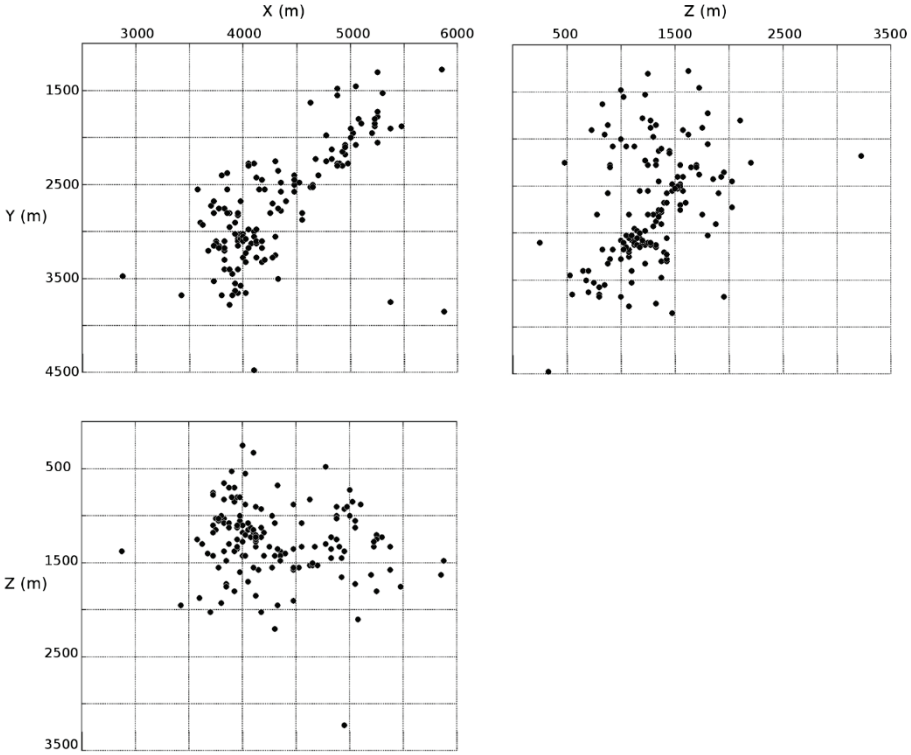

Figure A.12: Localization results in top and side views in the local coordinate system (see figure A.3). Depth datum is set to sea level.

A-6-5 Effect of Velocity variations

It is worthy to compare the migration-base localization results to those gained previously for the same dataset. Since only the location results of some of the events located by Wismut GmbH were accessible, the comparison could

not be done for all of the located events. On the other hand, in order to test the effect of velocity variations on the localization results, the localization algorithm is applied using two different P-wave velocity models to this part of the dataset; a constant velocity model of 6000 m/s and the 3-D velocity model. The localization results provided by Wismut GmbH were located using a 1-D station-based velocity model. This station-dependent model can be considered as a pseudo-3D model as it can account for some local velocity variations.

The comparison is illustrated in figure A.13. In x-y plane, the located hypocenters using the 3-D velocity model show a relatively fine adjustment in their location comparing the locations provided by Wismut GmbH, where the events are moved in y direction. Larger differences can be seen in the z direction. Here the results from 3-D velocity model are more extended in the z direction while the Wismut results are (except one event) concentrated within 300 m in depth (-1000 to -1300 m). A group of hypocenters located using the 3-D velocity model correspond to a rather vertical structure in x-z plane (the dashed box in figure A.13) while they are concentrated around a point in Wismut results (at down-left side of the dashed box in figure A.13). This obvious structure will be discussed in section A-7.

The velocity variations included in the 3-D model produce significantly different locations in comparison to the constant velocity model hypocenters. The differences are more distinct in the z direction where the results from the constant velocity model are located significantly shallower. This can also be seen when comparing the constant velocity model results to those from Wismut GmbH.

The average P-wave velocity in the 3-D model down to the maximum depth where the events are located (~-1500 m) is less than 6000 m/s, which is used

in the constant velocity model. But surprisingly, the events are located shallower when the constant velocity model is applied. A faster velocity should lengthen the calculated raypaths and locate the events deeper. On the other hand, the detected origin times (using the constant velocity model) are mostly later than the ones detected by applying the 3-D velocity model. This may explain the shallower calculated depths but cannot explain the hypocenters locations, which are scattered far away from other results also in the x-y plane. Nevertheless, the 6000 m/s is an accepted assumption for the constant velocity in this area. Migrating reflection seismic data using this constant velocity yields comparable results to the migration using the 3-D velocity model with small downward shifts in the position of the reflectors (Hloušek et al., 2015).

The migration procedure is much more sensitive to the accuracy of the velocity model in the case of earthquake location than when it is applied for reflection seismic imaging. In the case of reflection seismic data processing, most of the errors due to the inaccuracy of the lateral and vertical variations in the velocity model will be weakened during stacking since the wrong intersections of migration isochrones cannot be stacked constructively. Furthermore, for earthquake location the zero (origin) time is unknown and the data must be iteratively migrated over different assumptions of origin times. Thus, the errors in the constant velocity model can lead the migration isochrones to intersect with a maximum amplitude at the wrong zero (origin) time and spatial coordinates. This means that even moderate errors in the velocity model may cause significant shift in the location results. Thus the results of the constant velocity model are not reliable and only the 3-D velocity model is applied for the whole dataset. The focus of the analysis and discussion will be on the events located using the 3-D velocity model.

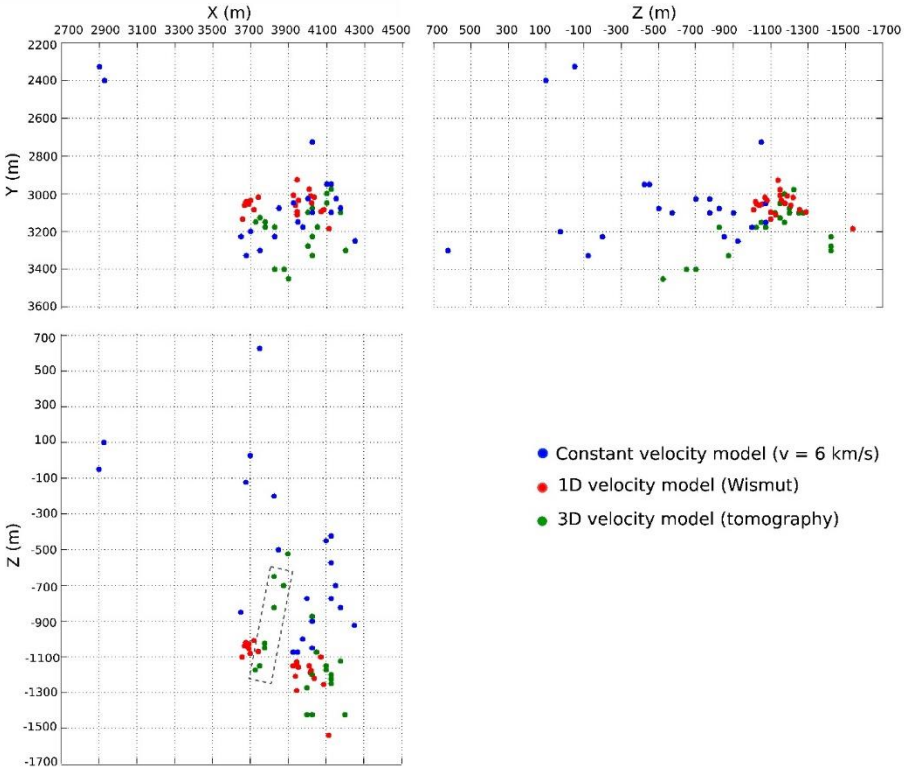

Figure A.13: Comparing hypocenters located with the constant velocity model (blue) and the 3-D velocity model (green) using earthquake migration (after Hassani et al., 2018). The hypocenter locations provided by Wismut GmbH, which they calculated using a station-dependent velocity model, are also shown for comparison (red). The differences are most significant in depth as can be seen in the two side views. Depth datum is set to sea level. The cluster of green hypocenters that are shown in the dashed box in the x-z plane are events which correlate temporally. This comparison is done only for a part of the dataset.

A-7 Results analysis

Seismicity is a known consequence of mining activities, usually associated with the removal of material. Furthermore, in mines prone to flooding, the increased pore pressure caused by the incoming water reduces frictional forces within fractures and decreases the fault strength. During mining operation, excavations cause disturbances in the mechanical state of the crustal structures and this stimulates accumulated shear stress in the rocks where the presence of either faults or weakness points potentially can cause stress release. Rockbursts and microearthquakes are common stimulated seismic events in mines during mining operations. Stronger seismic events can also happen as a consequence of the excavation-resulted stress inhomogeneity in bed rocks, e.g. the relatively large event which occurred in Schlema-Alberoda during mining operation (see section A-2-2). If the accumulated stress is not sufficient to overcome the shear strength of the structures (but comparable to this strength) during the excavations, it can cause earthquakes after the end of mining operation in the presence of any later mechanical disturbance. This can be either tectonic forces or an increase in pore pressure of crustal structures. In Schlema-Alberoda, several faults exist within the mine which extend down into the granite. These structures act as weakness points in the solid rock and stresses accumulated during the mining operation and subsequent flooding are preferentially released along these faults.

In order to monitor the geomechanical effects of the excavations on the crustal structures during mining operations in Schlema-Alberoda, some measurements were conducted to indicate the pressure variations on the bed rock. An ultrasonic measurement on the granite shows that the S-wave velocity increased from 3000 m/s in year 1982 to 3200 m/s in 1987 (Brinker,

2003). This is an indication of noticeable changes in the mechanical status of the crustal structures which is a consequence of the accumulated energy that can lead to triggered microseismic events by any later changes in pore pressure. On the other hand, several rockbursts happened during mining operations. Figure A.14 shows the occurrence frequency of these events. The first major rockburst happened in 1961 and until 1978, only 4 other rockbursts occurred within the mine. From 1979 to 1986, over 200 rockbursts were observed in the Schlema-Alberoda (Petschat, 1986). An interesting feature about these rockbursts is the dramatic increase in the number of events in this period of time (figure A.14). It is noticeable that these frequent rockbursts started after a relatively large magnitude (M_L=2.9) event in 1979 which obviously triggered successive stress releases. The frequent occurrence of these events after an idle period is an indication of rising inhomogeneity in the crustal loaded mechanical forces as a result of mass removals.

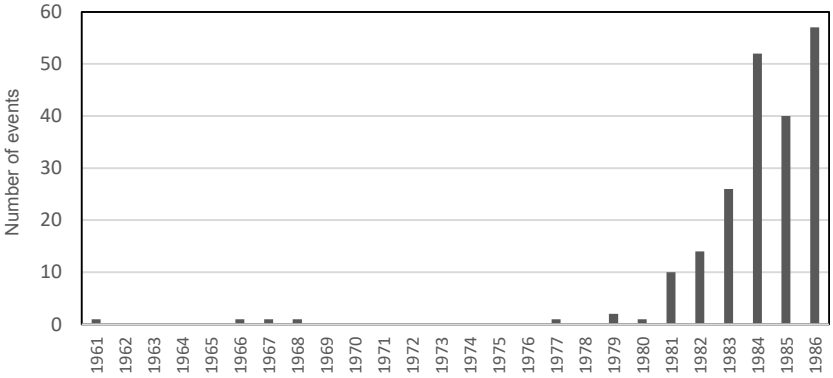

Figure A.14: Occurrence frequency of the rockbursts in the mine Schlema-Alberoda from 1961 to 1986 (after Petschat, 1986).

Referring back to figure A.13, within the events located using the 3-D velocity model, a group of the hypocenters are scattered almost vertically at the left side of the cluster in y-z plane (dashed box in figure A.13). These events correlate temporally as they all occurred within 14 hours. These hypocenters lie directly beneath the top of the granite under the Ruhmvoll fault and correlate with its interpreted extension (intersected by Bad Elster fault) into the granitic body (see figure A.2), thereby confirming its existence. Other localization results (Künzel, 2013) show that many events are concentrated along the interpreted extension of the Ruhmvoll. Wallner (2009) also shows evidence of the Ruhmvoll fault extension downward to the Roter Kamm fault.

Figure A.15 shows the located hypocenters projected on the 3-D seismic image of the area developed by Hloušek et al. (2015). As can be seen, the events are located along and (mostly) below the top of granite. The excavated area of the mine is located directly above the granite and some of the hypocenters, which are themselves located above the granite. The dispersion of the hypocenters indicates that these events are likely rockbursts that occurred within the mine openings. In the x-y plane it can be seen that all events are located within the mine area (figures A.12 and A.15) and their trend follows the extension of the excavations. This indicates that the located microearthquakes are stimulated events and in the presence of flood water in the mine, the accumulated stress releases at weakness points, since the flood water itself is also a source of stress induction. During flooding, mine pits act as new hydraulic connections which can increase the pore pressure in the preexisting fractures and faults below the mine and consequently trigger earthquakes.

Moreover, as discussed in section 1, historic observations show that this area is tectonically active. Due to the removed load during mining operations in Schlema-Alberoda, any small changes in the tectonic forces can easily trigger

the faults which are located below the mine. Consequently, this extends the size of the existing faults or can create new fractures. The clustered style of the located hypocenters can be an indication of crack growth and the release of the accumulated shear stress at the new cracks.

As can be seen in figure A.15-a, the hypocenters are mostly located between the top of the granite and the Roter Kamm, where several reflectors visible in the 3-D seismic image are located near to and parallel to the hypocenter clusters (figure A.15-a). However no clear reflections can be seen within the area where the hypocenters are located (figure A15-b). Nevertheless, the reflectors may in fact extend towards the area where the hypocenters are focused, indicating that the stress release happened along the reflectors but due to the very low reflection coefficients, this part of the reflectors cannot be detected in the 3-D seismic image. However, the frequency of energy release at this particular area between the top of the granite and Roter Kamm characterizes this area as an unstable zone.

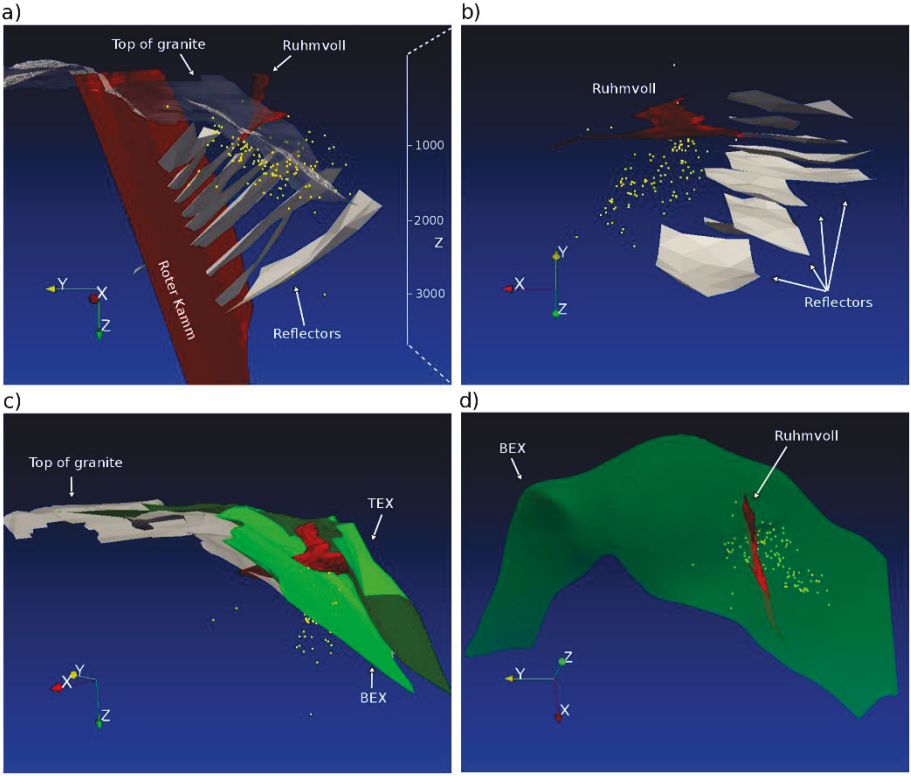

Figure A.15: Hypocenters plotted with the interpreted reflectors and known geology. BEX and TEX are the bottom and top of the excavated area. The Z axis shows the approximate depth at the vertical profile which crosses the middle of the area where hypocenters are located. (a): The hypocenters mostly concentrate directly below the top of the granite. (b): A cluster of hypocenters is located directly below the Ruhmvoll fault and follows an extension pattern, which seems almost the same as Ruhmvoll. In the 3-D image, visible reflectors do not extend to the hypocenters but are oriented towards them. (c) & (d): Some of the hypocenters are located between the top of the granite and the bottom of the mine (BEX) and few of them are within the mine.

A-7 Conclusions

The Kirchhoff Prestack Depth Migration algorithm provides high precision for locating microseismic events using only P-wave arrival times when an accurate velocity model of the area is available. The accuracy of this method is sensitive to the lateral and vertical variations of the P-wave velocity. Therefore applying a homogeneous velocity model even with a proper assumption of the average velocity may lead to unreliable results.

The results show that the flood water in the tunnels increases the pore pressure in the preexisting faults and discontinuities below the mine and stress release occurs due to the instability in the mechanical status of the crustal structures caused by changes in the volume and load. Also, the history of the seismicity in this area proves the existence of tectonic shear stress in the preexisting crustal structures causing (micro-) earthquakes which are triggered by any increase in pore pressure. The scattering pattern of the hypocenters proves the assumption that the Ruhmvoll fault has a downward extension deep into the granite. The deepest located hypocenters emphasize that new fractures are created within the granitic body far below the excavated area, some of them towards the Roter Kamm. These fractures are potentially new hydraulic connections which may cause new seismic events in deeper parts within the granitic body, especially in the case when the flooding level in the mine increases.

Comparing the localization results with the 3-D reflection seismic image where the reflectors are aligned between the top of the granite and Roter Kamm fault (figure A.15-a), a connection between the reflectivity and the located hypocenters is obvious. Although the visible parts of the reflectors do not reach the hypocenters position (figure A.15-b), the localization results can confirm their extension to the area where the hypocenters are located. Thus

the reflectors intersect with the Ruhmvoll fault and extend the fault plane down to the Roter Kamm.

In order to have a precise overview on the origin of the microseismicity in this area, locating more events over specific time periods will provide more detailed information about the main cause of the events by comparing the spatial focus of the hypocenters over different time periods. Also, real time monitoring using KPSDM method is useful for further studies on the seismicity of the area.

The 3-D velocity model used in the migration-based localization procedure does not account for the anisotropic properties of the phyllites and schists. Regarding to the tested accuracy of the velocity model (section A-6-3) no significant changes in the located hypocenters are expected. Nevertheless, developing an anisotropic 3-D velocity model of the area and applying it in the KPSDM localization algorithm would certainly strengthen the accuracy of the results.

The data used in this study contained only vertical component records. If three-component data would be available together with an accurate S-wave velocity model, S-wave arrivals can also be used by the designed localization algorithm and it may improve hypocenters location precision.

Interim summary

Usually in seismic exploration, imaging subsurface structures is conducted through conventional active seismic imaging methods using artificial seismic sources (explosives, vibro-trucks, etc.) and by installing a temporary array of receivers (geophones). In contrast, in passive seismic imaging methods, data collection is performed using mostly permanently installed seismic stations, and earthquakes as natural seismic sources. This will reduce costs of the survey and in some cases can be more effective and advantageous in comparison to conventional active seismic methods.

In chapter A, several microearthquakes are located in the Schlema-Alberoda mining area. Due to the reliable accuracy of the localization results (the spatial coordinates of the hypocenters and the origin times), the located events are appropriate to be used as natural sources for imaging local crustal structures in the area.

The recorded waveforms and the magnitude of the located events show that these events are originated from small-scale sources. Therefore, imaging structures in short distances from the hypocenters is feasible because the reflected waves from those structures are not distorted by direct waves. Also, the located hypocenters are focused directly beneath the mine, in an immediate vicinity of the crustal structures and in a favorable position with respect to the illumination angles of the structures. On the other hand, the hypocenters are located in the depth of 300-3200 m below sea level and are mostly concentrated within the granitic body beneath the mine. The low attenuation of the granite causes less energy loss, thus also reflections from boundaries with low acoustic impedance contrast are likely to be imaged by using these events as seismic sources.

In Chapter B, a subset of the recorded waveforms from the located microseismic events is used directly in a proposed passive imaging algorithm for two purposes; to test the functionality and effectiveness of the passive seismic imaging approach and to achieve a better understanding about the subsurface structures in the area. The results are then compared to the previous active seismic image of the area (see section A-7) to evaluate their accuracy and reliability.

B. Imaging crustal structures using microseismic events

B-1 Introduction

Conventional methods in reflection seismic imaging are widely in use to image subsurface structures either in shallow or deep seismic surveys where artificial sources (e.g. explosives, dropping weight and vibro-truck) are used to generate body waves. These methods are known as "Active Seismic Imaging" (ASI) and are well developed in seismic exploration industry. An alternative to the conventional ASI methods is "Passive Seismic Imaging" (PSI) where natural seismic events are used as energy sources and records of these events are used in imaging procedure. PSI is still not well established as a conventional method for imaging subsurface structures, nevertheless it has some advantages which makes it in some cases more effective than conventional active methods, e.g. less costs of data acquisition. In PSI, data acquisition is (in most cases) almost free of costs because the data are recorded by permanent seismic monitoring networks and the energy sources are natural.

Besides that PSI is cost-efficient, it also has some other advantages in comparison to active seismic techniques such as greater source energy, less attenuation in body waves and source distribution with no topographical limitation (Soma et al. 2002) which enables one to image reflections from deeper structures. On the other hand, when the target structures are located beneath the top of granitic basement, in most cases, active seismic methods

may not result in a detailed image (Asanuma et al, 2011). This of course depends to the acoustic impedance contrast at the upper boundary of granite and depth of the target as well as the attenuation of the body waves in overburden layers.

Nevertheless, PSI methods have their limitations and might be challenging to be applied. For instance, the position and distribution of sources with respect to target structures as well the frequency of occurrence and the magnitude of events. The latter is important with respect to the distance between a source and a target structure. Large events may not be proper sources for imaging reflectors which are located in the vicinity of the source because reflections will be distorted by direct waves.

A specific attribute of passive reflection seismic methods is their ability to image near vertical structures which makes them advantageous in the cases where target structures are steeply dipping. Reshetnikov et al. (2010) used microseismic events at San Andreas fault system to image near-vertical reflectors in the vicinity of a borehole by Fresnel volume migration (Buske et al, 2009). The final image is then compared to the results of the active seismic surveys in the same area and showed a significant improvement in the resolution of the imaged near vertical reflectors.

So far, different attempts and methods has been carried out to produce an image of the subsurface using non-artificial seismic sources. Daneshvar et al. (1995) used direct waves of microearthquakes recorded at the surface to detect the near-surface structures. In this method, near vertical incidence records were used. The autocorrelation of the transmitted (direct) waves from different sources recorded at individual stations showed a consistency to the acoustic impedance contrast of the shallow structures. Autocorrelation of transmitted wavefields represents the earth's transmission response which

is equivalent to surface zero-offset reflection records (Claerbout, 1968).

Soma et al. (2002) applied a passive reflection technique in which the 3D particle motion detected at a recording station (hodogram) is analyzed to find coherent signals and detect reflected waves which are covered by the direct wave coda. This technique which is called "AE (Acoustic Emission) reflection method" is performed for high-frequency signals (around 200 Hz). The imaging is conducted using S-wave reflections and its directivity with respect to the linearity of the 3-D particle motion. This technique is advantageous as it is able to detect reflectors using even one downhole 3-component if the source distribution is wide enough considering the target area. Asanuma et al. (2011) proposes a passive imaging method with same concept as AE, using a group of microseismic events which have similar waveforms, so called "microseismic multiplet". In this approach, hundreds of microseismic events are used and the advantage of waveform similarity and delays between reflected energy from different sources eliminates artifacts in the final image.

Presumably, in PSI for near surface structures, the sources are triggered or induced microseismic events, or natural microearthquakes which occur only as a result of pure tectonic pressure on active faults. Stimulated (induced and triggered) microseismic events are frequent phenomena in mining areas and hydrocarbon reservoirs (McGarr et al., 2002) due to excavations or changes in pore pressure.

When some prerequisites (e.g. availability of a reliable velocity model) are assured, it is possible to apply prestack depth migration techniques, which are usually used in active seismic imaging, also for PSI. In this study, subsurface structures in the Schlema-Alberoda mining area are imaged through a 3-D passive reflection imaging approach using the microseismic events which are located through the migration-based algorithm (chapter A).

The final image is then compared to the results of the active seismic survey conducted previously in this area.

B-2 Subsurface structures in the investigation area

In the Schlema-Alberoda mining area, the subsurface is structured by heterogeneous crystalline rocks (Hiller and Schuppan, 2008) and as discussed in section A-2, the area is located along the Gera-Jàchymov trans-regional fault zone. Several faults belonging to this fault system dip into the crystalline rocks at angles between 50° and 70° towards the south-west and are conjugated to the Roter Kamm (e.g. see figure A.2). These faults are vein structures and known as ore bearing veins since they are mineralized within the Silurian/Devonian schists in the mine. Displacements at the top of the granite caused by these "conjugate faults" makes the assumption of their extension to larger depths likely. The thickness of these conjugate varies between 10 m within the mine and up to 60 m in the granitic body.

The thickness of the Roter Kamm is 20-25 m and at some parts increases up to 100 m. On the fault plane, different veins are formed such as granite apophyses, aplite dykes and all formations of hydrothermal veins of different ages. The fault plane dips towards the north-east and likely extends to a depth of 8 km, as estimated through geological investigations during the mining operation.

B-2.1 Imaging significance in Schlema-Alberoda

As a major structure in the area, the Roter Kamm is a very important fault,

not only because it can cause earthquakes, but also the possibility of using this fault for geothermal energy exploitation. During mining operations in Schlema-Alberoda, one of the operations which became necessary was cooling the mine pits because the natural air circulation was not efficient enough to bring the temperature down to a level in which working would be possible (Hiller and Schuppan, 2008). For example, at a depth of 1270 m the rock temperature reaches up to 50 ^{o}C. Measurements showed that at depths between 500 and 1500 m, the temperature rises with an average rate of 0.035 ^{o}C/m (Korobko and Grebenkin, 1960). It is expected that the rock temperature reaches 160 ^{o}C at 5 km depth. The hot rocks (petrothermal reservoir) at this depth can be used as a source of energy (petrothermal reservoir). A conventional method for exploiting geothermal energy from petrothermal reservoirs is fracturing rocks by fluid injection in order to increase hydraulic permeability. Fracturing deep rocks can be a risky operation since it stimulates seismic events which can be large (see McGarr et al., 2002; Häring et al., 2008). An effective alternative to fracturing is using existing faults as hydraulic paths for exchanging heat in deep rocks.

Since the Roter Kamm is geologically interpreted to extend down to a depth of 8 km, it can be an ideal hydraulic path to exchange geothermal heat. However, for that purpose, the fault plane must be precisely imaged to ensure its extension and path. Other smaller faults in the area such as conjugate faults are also important in this aspect to be imaged precisely.

Imaging the aforementioned structures is challenging since they have steeply dipping angle and are in a crystalline environment. Small scale heterogeneities within crystalline rocks cause significant diffracted and scattered energy which can affect the accuracy of the seismic image unless an appropriate migration method is applied. Kirchhoff prestack depth migration (KPSDM) is an effective migration method for imaging structures

within crystalline rocks because it is a diffraction summation based method that uses only first reflection arrivals. Therefore it is able to efficiently construct diffraction surfaces. On the other hand, the KPSDM method has no initial assumption about the slope of the structures which makes it advantageous especially in crystalline environments (Buske, 1999).

B-3 Principle of 3-D coherency migration

A disadvantage of Kirchhoff migration is that the amplitudes smear along the TWT (two way traveltime) isochrones (see section A-5-2). This can be problematic where the sharp angles in crustal structures are to be imaged and also when the interval between receivers is not small enough to build up reflection surfaces. To avoid the smearing problem, one may apply a migration aperture which images the reflected wavefield within a certain angular limit. This however will affect the resolution of the migration results at shallow depths and also restricts steep structures from being imaged. In this study, applying a migration aperture is meaningless because of the low number of receivers (see section B-4-1) and also that the position of sources and receivers does not give a wide coverage on the studying area.

An effective solution to avoid wavefield smearing in KPSDM is to take the coherency of the recorded amplitudes into account. Neidell and Taner (1971) introduced a coherency measurement as a "semblance coefficient" for a single shotgather which evaluates the coherency between the amplitudes in neighboring traces. Here, an additional weighting factor is applied to the KPDSM based on the semblance coefficient to focus the amplitudes onto the real physical diffraction points in depth during wavefield summation. Coherency migration (Hloušek et al., 2015) can be defined as:

$$I(m) = \frac{-1}{2\pi} \int_A \int C_s(m,r) w(m,r) \frac{\partial}{\partial t} u(r, t_s + t_R) dr \qquad [5]$$

The term $C_S(m,r)$ is the weighting function which represents the semblance coefficient as

$$C_S = \frac{\int_{-T/2}^{T/2} \left| \sum_{i=1}^{N} u_i\left(t + t_s + t_{r_i}\right) \right|^2 dt}{N \int_{-T/2}^{T/2} \sum_{i=1}^{N} \left| u_i\left(t + t_s + t_{r_i}\right) \right|^2 dt} \qquad [6]$$

This function is defined for each image point m and each receiver r in a shot gather and represents the coherent energy of the wavefield in relation to its total energy within a defined time window T and over N neighboring traces. The length of the time window T must be chosen based on the source signal length. In practice it is equal to the length of the phase which is to be imaged (e.g. P-wave). The coherency ratio (eq. 6) varies between 0 which means no coherency (i.e. random noise) and 1 when the wavefield is perfectly coherent. Thus the smearing of the amplitudes will be limited to the physically contributing part along the migration operator (TWT isochrone), i.e. the diffraction point.

The principle of Coherency migration is visualized in figure B.1. Suppose that the diffraction point D lying in a constant velocity medium is to be imaged using a source located at depth and an array of receivers on the surface (figure B.1-a). If the source releases a single wavelet, the resulting diffracted wavefield recorded by the receiver array would be like as shown in figure B.1-b. The dashed ellipsoid in figure B.1-a is the TWT isochrone ($t_s + t_R$) corresponding to one receiver (blue). Migrating this single trace through KPSDM smears the recorded wavefield along the whole TWT isochrone

(figure B.1-e) and all of the points on the isochrone will be introduced as diffraction points. Applying coherency migration to the record of the aforementioned single receiver using 10 neighboring traces (5 traces on each side), the recorded signal (the blue trace) gains a high coherency factor (eq. 6) around point D during migration (figure B.1-f). This is because the recorded amplitudes at neighboring receivers are coherent due to the diffraction point D, i.e. they follow the calculated traveltimes pattern for point D within the defined time window T (figure B.1-b). In other words, one measures the semblance of the neighboring traces within the time window for a specific point. On the other hand, considering a hypothetical diffraction point D' on the TWT isochrone (figure B.1-c), the recorded amplitudes at the neighboring traces do not follow the calculated traveltime pattern for this point (figure B.1-d). Thus the coherency factor for this point is low and the imaged amplitudes will be decreased around it during migration (figure B.1-f). Therefore, in coherency migration, smearing of the migrated amplitudes will be limited around actual diffraction points and the resolution of the final image increases.

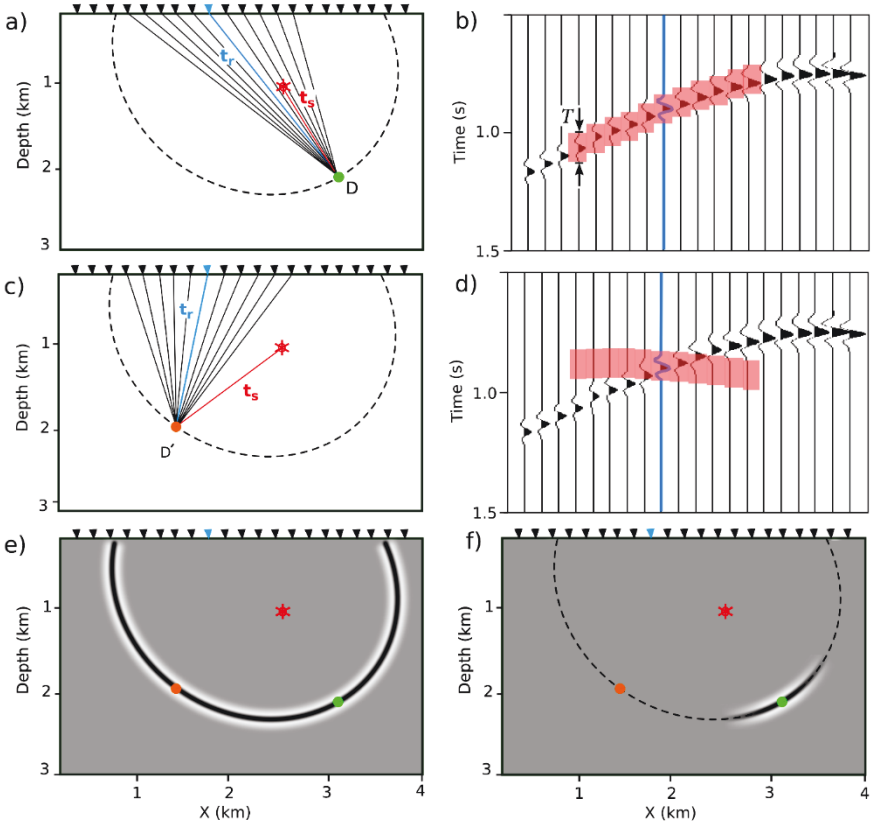

Figure B.1: The concept of coherency migration (after Hloušek et al., 2015). The red asterisk shows the source position and the triangles are the surface receivers. The red boxes in b and d are the time windows with the length T on the neighboring traces. For detailed description see text.

B-4 Imaging microseismic data

B-4-1 Data preprocessing and analyzing

For locating hypocenters, as described in section A-6-2, pseudo-synthetic seismograms were used to represent the manually picked P-wave first breaks. For imaging subsurface structures, the original recorded traces of the same dataset are used after applying the same filters as in localization procedure (see section A-4-2). In addition, to magnify the attenuated amplitudes reflected from deeper parts, the recorded amplitudes are gained by a time exponential factor of 2 ($A_{out} = t^2 A_{in}$).

Generally in passive seismic imaging, not all recorded traces may be appropriate for the imaging procedure. Although 135 events are located with a reliable accuracy, only those source-receiver pairs with maximum S/N ratios are selected in order to achieve a maximum precision in imaging, only those source-receiver pairs are selected which have maximum S/N ratio. Also, to eliminate borehole reverberations, the records of the two borehole hydrophones are eliminated in the imaging procedure.

In addition to the importance of the S/N ratio, the differences in the source mechanism and wave propagation patterns in PSI may introduce complications. One must analyze the dataset carefully and contribute only those parts of the data into the migration procedure which fulfill the requirements of the specific applied imaging method. Since the dataset contains only vertical component records, it was more meaningful to rely on only P-wave secondary arrivals (reflections) for imaging the subsurface structures. Thus the traces with clear and strong (in comparison to the maximum recorded amplitude) direct P phase are chosen for imaging. This

implies that the source released enough energy in the form of P-wave that the P-wave reflection amplitudes can overcome other phases in the traces which will be used in the migration procedure.

Due to the source focal mechanism and the disposition of the source-receiver pairs with respect to reflectors, it is possible that a source released enough energy in the form of P-wave, but the direct P-wave recorded at specific stations has a low amplitude. In such a case, the P-wave reflections from those reflectors which are located at a proper position to the source and receiver can be recorded efficiently to be imaged. Nevertheless, to use these records which may contain strong P-wave reflections despite the low-amplitude direct P-wave, focal mechanism analysis of the hypocenters is necessary.

These considerations led to a selection of 170 traces from about 5000 recorded traces. Due to the inconsistency in the recorded amplitudes at different stations and also different magnitude of the events, the traces are normalized to assure their equivalent contribution in the migration procedure. Figure B-2 shows an example of recorded (filtered) traces from one of the events and the selected traces among them for the imaging procedure.

Figure B-2: The recorded traces of an example event (a) and the selected traces for the imaging procedure (b). The red spikes are the picked P-wave arrival times used for locating the hypocenter (see section A-6).

B-4-2 Migration

Basically, the coherency migration functions over a single shotgather because the source signal must be similar between the neighboring traces through which the coherency value is to be measured (Neidell and Taner, 1971). The presumption is that all the receivers are identical in their physical properties (natural frequency) and they are attached to the same ground with the same rigidity so that the recorded traces would have similar frequency content. This condition is valid in almost all active seismic surveys and because normally the intervals between the geophones does not exceed some meters, the ground over which the neighboring geophones are installed has the same properties in the sense of wave propagation (e.g. density, porosity and weathering layer thickness). Thus there would be no significant difference in the frequency content between recorded wavefields at neighboring geophones due to attenuation.

However, in this study the recording network is not designed for a seismic survey and the receivers are attached to different grounds like solid rock, concrete based surface, weathering surface, etc. On the other hand, due to the distances between the recording stations (up to several hundred meters), the underlying layers (especially weathering layer) may vary for different stations. These cause differences in frequency content of the recorded source signal from a single event at different stations. Figure B.3 shows selected records of two single events (shot gathers). As can be seen, the recorded wavefield appears with different frequency content at different stations. Comparing the recorded traces between all shot gathers, a similarity in frequency content as well as waveform between the records of different sources at individual receivers could be identified (figure B.3-c). Therefore, for this dataset it is more relevant to apply the coherency migration to common-receiver gathers.

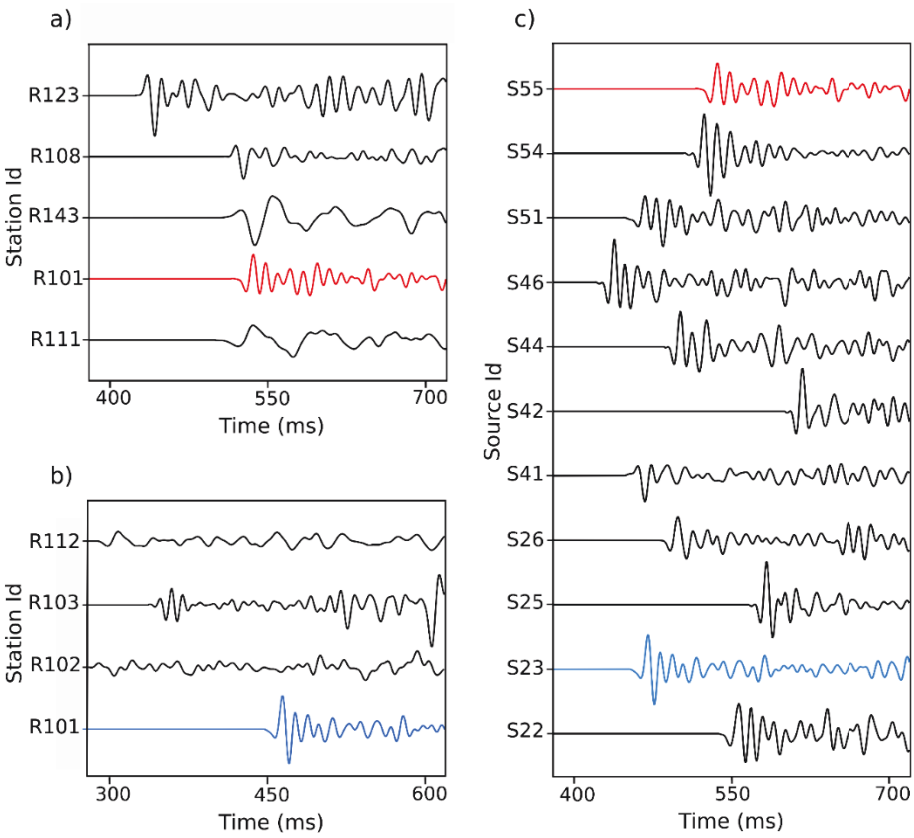

Figure B.3: An example of two common-source gathers (a and b) and the common-receiver gather R101 (c). The red and blue traces are recorded from the events S55 and S23 by the station R101 respectively. The total record length is longer than that shown time window. The order of the records in source gathers is as stored in the dataset.

Due to the criteria for choosing proper traces for the migration procedure, the selected data was grouped into 30 receiver gathers. Referring back to the equation [6], more neighboring traces (N) used to compute the coherency value, result in a more accurate measurement. Generally, this value (N)

should be selected by also considering the computation costs. In order to achieve a reliable coherency measure, only those receiver gathers with at least 7 traces are used. Finally 10 receiver gathers including records from 48 sources with a total number of 128 traces were chosen for the migration. The receiver gather with the largest number of traces contains 26 sources. During migration, all traces in each receiver gather are involved in calculating coherency factors as neighboring traces.

After evaluating the direct P-wave wavelength in all traces involved in migration procedure, each receiver gather is assigned an individual length (varying between 16 and 42 ms) for the time window T over which the coherency value must be calculated (see eq. 6). In order to avoid the effect of the varying focal mechanism on the polarity of the recorded wavefields, the traces are adjusted to the same polarity.

To magnify the focusing effect of the coherency migration, an exponent $\propto$ can be applied to the coherency function in equation [5] as $C_S^{\propto}(m,r)$. A higher value of $\propto$ intensifies the most coherent amplitudes and suppresses the less coherent ones and random noise. To avoid exaggerating the coherent signals and the resulting ghost reflectors by choosing a too high value of $\propto$, different values must be tested to find the optimum one. Here the $\propto$ value of 3 is used in the coherency migration.

For calculating traveltimes, the same method as in the localization procedure is used (finite difference approximation of the eikonal equation – see section A-6-3). Since the traveltimes are calculated based on the P-wave velocity, it is expected that the coherency factor measured for S-wave reflections is low and through the exponent value $\propto = 3$ for $C_S^{\propto}(m,r)$, the reflected S-wave amplitudes are decreased during the migration. This can assure that only P-wave reflections are the dominant constructive migrated amplitudes in the

final image.

B-4-3 Results and discussion

As described in the previous section, the prestack coherency migration is applied to the receiver gathers resulting in an individual image for each single receiver gather. A final image is then obtained by stacking these single images.

To obtain a migrated image, different methods can be applied such as migrating the envelope, absolute values or real values of the wavefield (phase-consistent image). In this study, the absolute and real values of the wavefield are used to image the receiver gathers. To reduce the effect of amplitude distortions due to the presence of the S-wave and its reflections and reverberations, the coherency value calculated during migration, is also considered as an image value. The resulting image is called as “coherency image” in following.

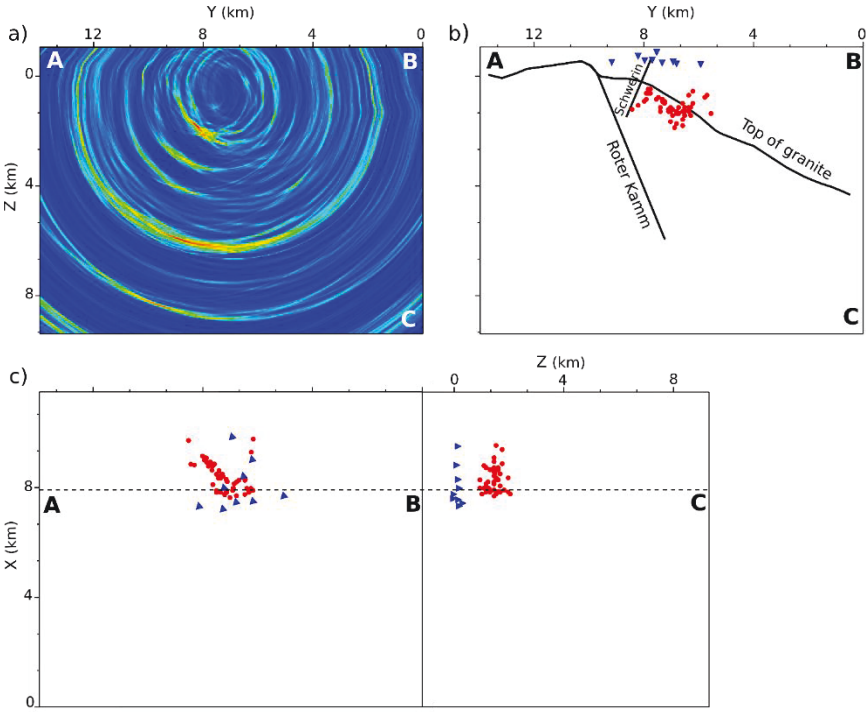

Figure B.4: a) A vertical slice through the 3-D coherency image. b) The same slice as (a) showing major structures mapped in geological surveys and the sources (red circles) and receivers (blue triangles) contributed in the imaging procedure. c) Top and side views of the 3-D model; the dashed line ABC refers to the position of the image slice in (a).

Figure B.4 shows a vertical slice through the 3-D coherency image cube and the position of the selected sources and receivers used in the migration procedure. As can be seen, the sources and receivers have a limited coverage over the image cube. Therefore the analysis is focused on the parts of the image cube with near offset to the source and receiver positions. For comparison and further analysis, the size of the 3-D image cube is defined

the same as the 3-D image cube of the area recently obtained through an active seismic survey.

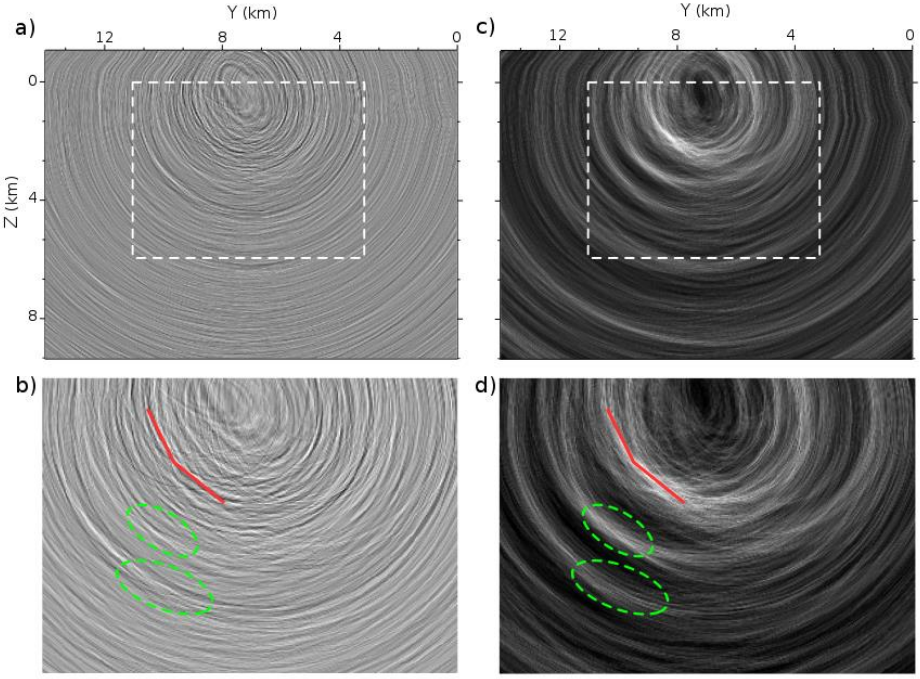

Figure B.5: Vertical slices through the phase consistent image (a) and absolute values image (c). The dashed boxes refer to the zoomed-in illustrations (b and d). The red solid line shows the imaged part of the Roter Kamm fault and the green dashed ellipses refer to the reflectors B and D in figure B.9.

Vertical slices through the absolute value and the phase-consistent image cubes are shown in figure B.5. These slices have the same x-coordinate value as the vertical profile in figure B.4. Comparing these three images, it is clear that the coherency image has a better resolution. Particularly, in the deeper

parts, some reflectors are visible in the coherency image which are not very clear in the two other images. However, one of the reflectors is clearly visible in all three image cubes in the shallower parts of the image close to the position of the sources (figures B.4 and B.5). This reflector will be later discussed in detail.

The S-wave presence with a comparable amplitude to the P-wave is a complication which affects the quality of the final image, especially when the absolute or real values are imaged. S-wave reflections cannot gain a high coherency value and because of the P-wave velocity model, the S-wave phases should not be added constructively during migration. However, these amplitudes still can appear in the final image and distort P-wave reflections. Besides that, in some of the events (sources), the S-wave has a lower frequency which causes less energy loss in its reflections from deeper parts in comparison to those of P-wave (figure B.6), therefore reflected P-waves from deeper parts can be covered by S-wave reflections.

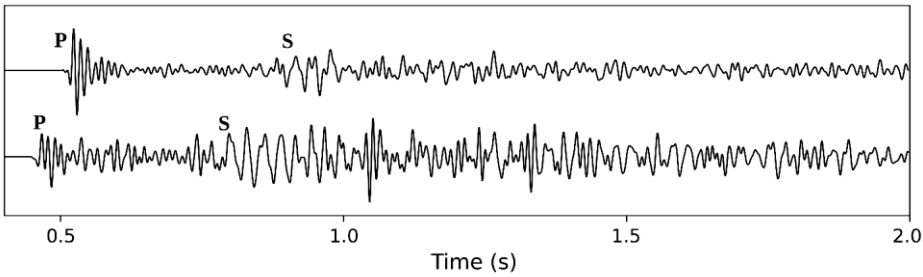

Figure B.6: An example of the waveforms used in the migration procedure. The P- and S- direct waves are marked for comparing frequency contents.

Nevertheless, since the coherency value is calculated over a time window which represents the P-wavelength, the S-wave and its reflections could have only a minimal contribution and the calculated coherency values are less affected by S-wave direct or reflected phases. Therefore the final image would be less distorted when the amplitudes are not directly included in the image. Thus the discussions and analysis will be mostly focused on the coherency image. Figure B.7 shows sequential vertical slices through the 3-D coherency image with an interval of 125 meters.

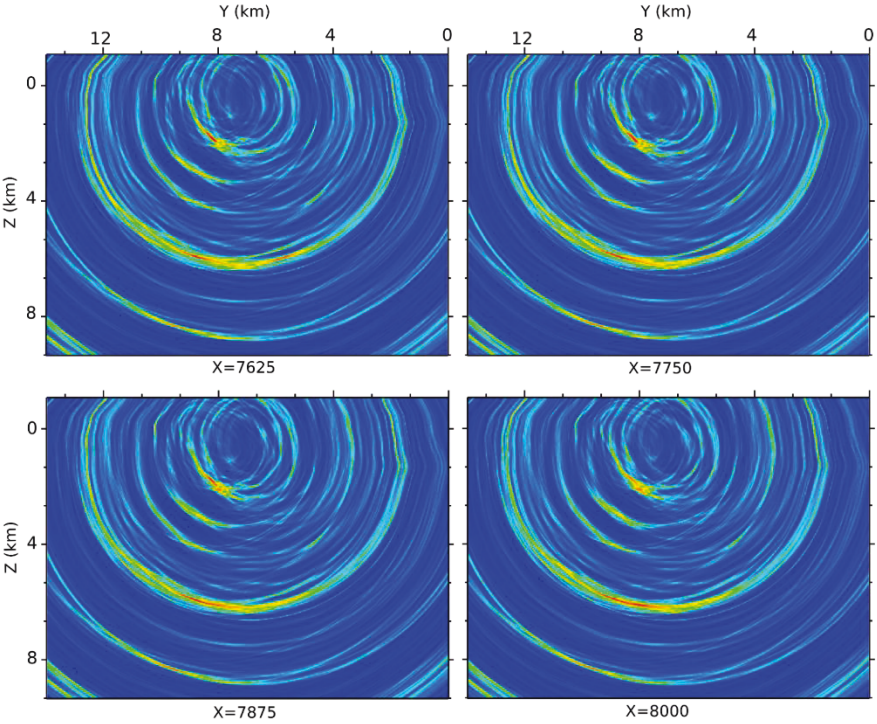

Figure B.7: Sequential slices in x direction through the 3-D Coherency image.

As described in section B-2, a major structure in this area is the Roter Kamm fault. The part of this fault observed through geological surveys reaches a depth of ~300 m below sea level and based on the properties of the area, it is expected that the fault plane has a linear extension down to a depth of 8 km. The final results of this study detects this fault which is clearly visible in the coherency image as well as the phase-consistent and absolute value images (figures B.5 and B.8). Nevertheless, the results show differences to the previous assumptions about the Roter Kamm's extension. The imaged fault plane has a slightly smaller dipping angle, it is bent at a depth of ~1400 m and it extends further towards the north-east (negative y direction in the local coordinate system) with a smaller angle down to ~2600m below sea level (figure B.8). A further possible extension of the fault plane could not be imaged due to the position of the sources and receivers. The Schwerin fault is another structure which was mapped during the mining operation in the area and was expected to intersect the Roter Kamm. Surprisingly it can be seen that this fault extends directly towards the bending point of the Roter Kamm. It is convincing that the Schwerin fault plane extension reaches the Roter Kamm, indeed at its bending point (figure B.8).

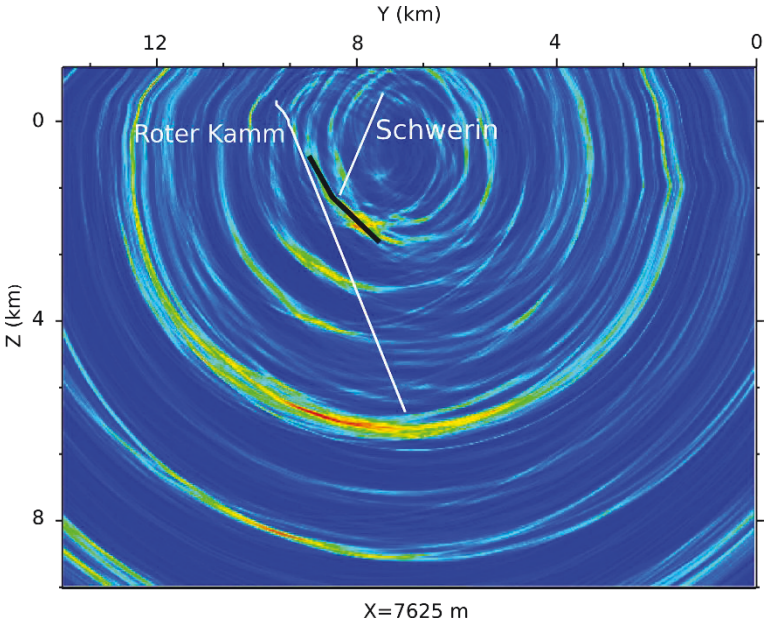

Figure B.8: Correlation of the coherency image with the extension of Roter Kamm and Schwerin marked in the geology map of the area. The solid black line emphasizes the imaged fault plane (Roter Kamm).

B-4-4 Evaluating the results

Recently, a 3-D active reflection seismic investigation was conducted in the same area and resulted in a 3-D image cube detecting several crustal structures (Hloušek et al., 2015). To compare the PSI results with the active seismic image cube, only the area under the coverage of source-receiver positions is considered. Figure B.9 shows the same vertical slice of the 3-D coherency image and of the 3-D absolute value image developed through the active seismic survey.

As mentioned before, the Roter Kamm fault is one of the structures which is visible in all three final images in this study, but in the active seismic image, the fault plane is not clearly visible. Generally, in an active surface seismic survey, structures with a large dipping angle are unlikely to be imaged unless the data contains records of far-offset sources and receivers and the target structure has a high acoustic impedance contrast (reflectivity) so that the body waves can be reflected with a minimum refraction at the reflector's boundary. This is however not a limitation in passive seismic imaging because the sources usually release more energy and are located underground, therefore with less energy loss. Thus if the receivers would be installed in a proper disposition, near vertical structures can also be imaged even if they are not strongly reflective.

The Roter Kamm is a vein structure (see section B.2) and according to its geological properties, the fault plane is not expected to be strongly reflective. In addition, this fault has a large dipping angle (figures B.5 and B.8). Thus the fault plane could not be imaged by the active seismic survey.

Nevertheless, Hloušek et al. (2015) show evidence in some parts of the 3-D active seismic image which demonstrates the existence of the Roter Kamm, e.g. discontinuities in some other reflectors (at a distance larger than 1.0 km to the analysis area of this study in x-direction). Also, in a part of the image cube, after stacking the shot gathers with a far-offset to the Roter Kamm, they could detect an acoustic impedance contrast at the area where the Roter Kamm is expected to be located.

Most of the reflectors detected in the PSI results are also visible in the active seismic image cube (Fig. 9). One of the structures detected in both images is the so called "Schneeberg Body" (SB) which is an unknown reflective zone in the depth of 4-7 km and its existence was detected first by the aforementioned

active seismic survey. Hloušek et al. (2015) give a hypothesis about the nature of the SB and describe it as a high reflective complex zone. This structure zone shows higher reflectivity at its top and bottom in the active image whereas in the PSI results, the top and bottom of the SB are clearly visible with distinctive amplitudes (reflectors D and F in figure B.9). Especially at the bottom of the SB, the less reflective dipping tail in the active image follows the trend of the detected reflection (F) in the passive image. Both images detect reflectors C and E, which have a lower reflectivity. These reflectors belong to a group of so called "conjugate faults" that extend towards the expected deeper extension of the Roter Kamm. The connection of these faults with the microseismicity in this area is discussed in section A-7.

Directly above the SB, a fairly strong and well-focused reflection can be seen in the coherency image (reflector B in figures B.9 and B.10), while in the active image, a structure oriented perpendicular to reflector B with low reflectivity is imaged at the same position. Figure B.10 shows a focused view of this reflector and compares it to the phase-consistent active image. As it can be seen, Reflector B correlates perpendicularly to the small-scale parallel reflections detected in the active image. This reflector can be interpreted as a small zone of mineralization related to the SB, nevertheless it is not connected to the uppermost layers. In figure B.10, reflector D also shows a very good correlation to the detected reflector at the top of SB in the active image. Reflectors B and D (top of SB) are also visible in the absolute value and phase-consistent images (figure B.5).

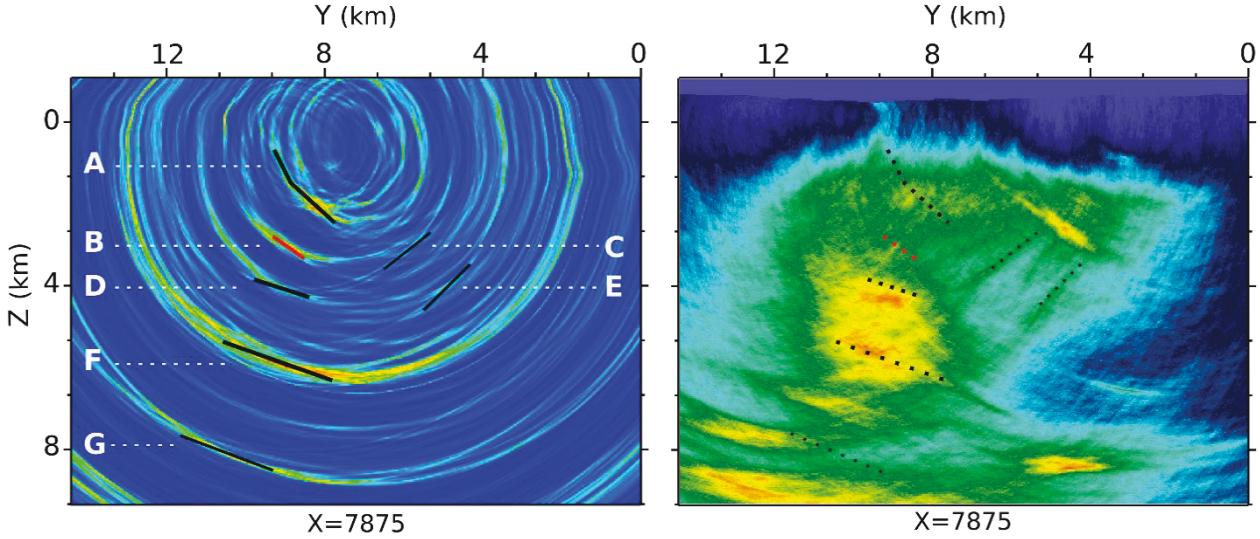

Figure B.9: Comparing the imaged structures (left) to the results of an active seismic survey in the same area (Hloušek et al., 2015) (right). The thick solid lines show the reflectors with higher image value and the thin solid lines show the reflectors with a lower image value and the dashed lines show them projected on the active image

In the deeper parts of the image cube, there is also a reflector (G) detected in the coherency image. Comparing to the active image, this reflector has a displacement in the negative Y direction. It must be noticed that in the dataset, the recorded traces were not in the same length and not all of them reach the deeper most part of the cube (in depth domain). Therefore, the resulted image has less accuracy at depths greater than 7.5 km. On the other hand, this reflector has an offset of ~5 km to the position of the sources and receivers which can also cause bias in the position and dip of the imaged reflector. Therefore the detected position of this reflector is more reliable in the active image.

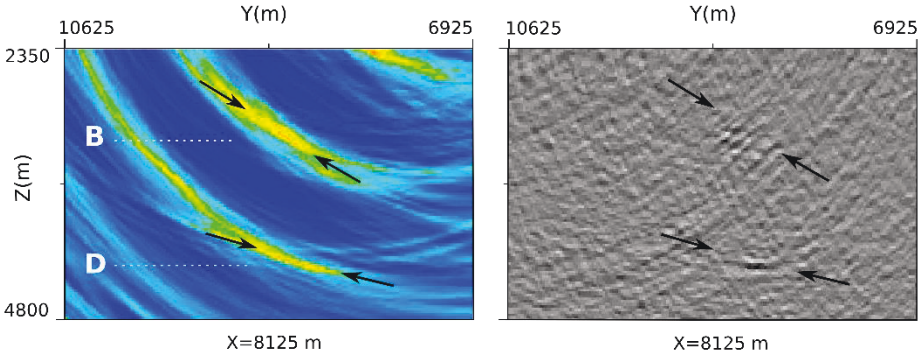

Figure B.10: A zoomed illustration of the reflectors B and D in the coherency image (left) and their position marked by the arrows on the same slice from phase consistent active image (right). Note that these slices are located in a distance of 250 m in x direction to the slices in figure 9.

B-5 Conclusions

In this chapter, a passive seismic imaging approach using the coherency migration technique is presented for imaging crustal structures using the records of one component (vertical) geophones. Despite the narrow aperture of the source-receiver positions, the accuracy of the results is remarkable.

As discussed before, the data used in this study was collected by a permanent local seismic monitoring network which is not designed for seismic surveys and therefore the dataset was not optimal for conducting a passive seismic imaging survey. Nevertheless, in spite of the low number of recorded traces which were appropriate for imaging the subsurface structures, the imaging procedure is designed and conducted so that the best possible accuracy in the results could be achieved. The results show that the coherency migration is an effective and powerful technique for imaging passive seismic data due to its focusing effect which can efficiently amplify P-wave secondary arrivals (reflections) and suppress random noise and other phases while migrating the data.

The final image shows a reliable match to the results of the active seismic survey conducted previously in the same area. In addition, the advantage of the passive seismic imaging led to a better understanding of some structures with low reflectivity such as the Roter Kamm and Schwerin faults. Furthermore, the correlation between the results of both passive and active imaging surveys demonstrates the reliability of both results.

The similarity of the recorded waveforms from different sources verifies a resemblance between the hypocenters. This is proof of the findings in the first part of this thesis on the nature of the current seismicity in the area. It is interpreted that most of the microseismic events beneath the Schlema-

Alberoda uranium mine have the same nature and are a sign of crack growth and the reactivation of preexisting faults in the granitic body due to the increasing pore pressure.

The position of the sources and receivers in relation to the source focal mechanism and the geometry of the structures (position, strike and dip direction), affects the recorded P-wave reflections at individual receivers (see section B-4-1). Based on the localization results (chapter A), most of the located events are expected to originate from the preexisting faults or new growing cracks and fissures in the granitic body. Regarding the position of the sources and receivers (figure B-4) and as it is obvious in the final image, the structures located at the left side (south-west) of the source and receiver positions are perfectly imaged. These structures dip towards the north-east (e.g. the Roter Kamm) and the P-waves released from the sources could be efficiently recorded by the receivers. Therefore, the P-waves must have been released from sources with a relatively perpendicular mechanism direction to those structures. This is proof of the previous interpretation that the preexisting faults and fractures (or new cracks) which are dipping towards the south-west in the granitic body (see figure A-2) are the origin of the events.

The velocity model used in the imaging procedure does not include anisotropic properties of the underlying crystalline medium. This velocity model is the same as the one used for the previous active seismic survey and its reliability is confirmed through tests by Hloušek et al. (2015). No significant bias is expected in the imaged structures although some minor errors might be included in the velocity model.

Summary

In this thesis, microseismicity in the Schlema-Alberoda mining area was investigated and some of the crustal structures were explored through a passive seismic imaging technique.

A localization algorithm based on Kirchhoff prestack depth migration was developed and several microseismic events that occurred between 1998 and 2012 are located in the area. The dataset contained only the records of one component (vertical) stations. The precision in origin times and hypocenters location is 2 ms and ~50 m, respectively. The localization results are compared (partly) to the results of a previous localization survey in the area; some adjustments in the location of the hypocenters could be identified which are convincing with respect to the geological properties of the area.

The located events in connection with geological information of the area show that the main cause of the current seismicity in the area is the increasing pore pressure in subsurface structures as consequence of the flooding. With respect to the seismologically active history of the area, the increasing pore pressure and the unstable mechanical state of the structures (as a consequence excavations), will cause more microseismic events and the occurrence of larger events is also likely.

The scattering pattern of the located hypocenters confirmed expected extension of pre-existing faults within the granitic body and also existence of new cracks and fissures. In particular, it is very likely that the Ruhmvoll fault is extended to the Roter Kamm fault plane. On the other hand, comparing the located hypocenters with the results of a previously conducted

active seismic imaging survey in the area, a relation between reflectivity and seismicity in this area is identified. Some of the imaged reflectors extend towards the located hypocenters and their slope correlates with the direction of the faults and fissures which are interpreted to be the origin of the located events. The slope of these reflectors together with the scattering pattern of the hypocenters confirms the connection between the so called “conjugate faults” (e.g. Ruhmvoll) and Roter Kamm.

In order to test the sensitivity of the localization algorithm to velocity variations, a constant velocity model is applied to a part of the dataset. The results show that the migration-based localization technique is sensitive to the accuracy of the velocity model and errors in velocities may cause significant shifts in the located hypocenters and origin times.

The located events are then used to image subsurface structures beneath the mine through a passive seismic imaging approach. For this purpose, after analyzing the dataset, some of the recorded traces from several events are selected and used in the imaging procedure. The imaging is conducted using P-wave secondary arrivals and by applying 3-D coherency migration technique, which is a focusing extension of Kirchhoff prestack depth migration.

The passive imaging results are compared to the images obtained from a 3-D active seismic survey conducted previously in the same area. Several reflectors which are detected by the active seismic survey are also visible in the passive imaging results. The comparison confirmed the accurate performance of the passive imaging procedure. This is also proof of the precision of the localization algorithm and the detected hypocenters and origin times.

Furthermore, the fault Roter Kamm, which was not clearly visible in the results of the active seismic survey could be imaged through the passive seismic approach despite its steep dipping angle and low reflectivity. The final image identified an adjustment in the previous geological interpretation of the fault plane extension. The fault dips into the granitic body with a smaller angle and bends at a depth of approximately 1400 m below sea level.

The imaging results confirmed the previously interpreted orientation of faults and fissures within the granitic body which extend relatively perpendicular towards the Roter Kamm. This supports also the aforementioned interpretations from the scattering pattern of the located hypocenters.

Analyzing the final image also showed that in a passive seismic approach, with respect to the imaging method and the reflected phases which are used for imaging, the source-receiver positions and the focal mechanism of the sources can affect significantly the quality and resolution of the final image.

Outlook

The presented study attempted to derive the best possible results from the available dataset and velocity model. The results of both parts of the study are satisfying as their reliability is proved from different aspects. The localization and imaging methods can be used for investigations in any other area, especially in areas with complex geology, the procedure can be useful to precisely locate microearthquakes and image subsurface structures.

Nevertheless, applying a 3-D velocity model which includes the anisotropic characteristic of the crystalline environment, may strengthen the accuracy of both the localization and imaging results. To improve the precision of both procedures in Schlema-Alberoda, It is recommended that the recording network be modified in two aspects. First, the installation condition (rigidity and spacing) of the stations, which can improve the quality and consistency of the recorded waveforms. Second, the coverage of the network over the area. An expanded recording network is highly recommended since this will extend the imaging aperture and consequently strengthen the accuracy and resolution of the imaging results, in particular, of the targets in deeper parts.

The dataset used in this study contains only 1-component (vertical records) and therefore, only P-waves are used in the localization and imaging procedures. Installing multi-component recording stations around the study area will provide the possibility of using S-waves in both procedures and can improve the results. Not to mention that generally in the case of natural seismic sources (earthquakes), a significant part of the energy releases in the form of S-wave.

The released energy from the seismic events in Schlema-Alberoda in the

presence of tectonic forces and overburden load, may result in deformations and breakdowns in the mine openings and pits, which consequently can cause collapses in larger dimensions with destruction at the surface. The results of this study show that the occurrence of seismic events will continue and therefore, permanent and precise seismic monitoring in the area is imperative.

Locating more events within individual time periods with the presented localization algorithm may provide more details about the fault extensions and fractures and crack growth within the granitic body. The resulting information can be valuable for anticipating upcoming events. On the other hand, through such a survey, new hydraulic paths can be detected (particularly in connection to the Roter Kamm) which may be useful in a geothermal project.

The imaged part of Roter Kamm demonstrated its reflectivity and therefore proved mineralization on the fault plane within the granite (at least partly). It is recommended that by installing recording stations (preferably 3-component) at far offsets to the fault plane, and distributed over the north-eastern part of the area, another passive seismic imaging survey would be conducted using the same approach as in this study. It is expected that through such a survey, the fault plane can be imaged in more details including its likely downward extension.

Acknowledgements

First of all, I want to thank Prof. Dr. Stefan Buske who gave me the possibility to do my doctorate and who was my doctoral supervisor. He gave me continuous guidance and support for my work and was always available for questions and discussions. He provided me full access to his developed codes and his previous work. His expertise in processing and prestack migration techniques contributed significantly to my research. Beyond his scientific support, he employed me for the most of the period of my doctoral research.

Special thanks to my colleagues Dr. Felix Hloušek and Dr. Olaf Hellwig who were very supportive and provided me great help during my research and spent a lot of time for discussions. The Coherency migration technique that I used in my research is developed by them. Felix was also a coauthor in one my publications.

I'm very grateful to Dr. Catherine Alexandrakis for her support and help during my work. Besides that, she spent a lot of time for editing my thesis text for English and. She was also a coauthor in one of my publications.

I also want to thank Falk Hänel, another colleague of mine in TU Freiberg for the information he provided and the discussions about the seismicity and seismic network in Schneeberg.

I thank Dr. Olaf Wallner (Wismut GmbH) and Mr. Thomas Ebert (C&E GmbH) for providing the data which I used in my research.

I would also like to thank Prof. Dr. Michael Korn who agreed to be the second reviewer of my thesis.

Finally, I'm very thankful from the deep of my heart to my wife, Dr. Arezoo Mirzaei, who was very patience and always there for me during my doctorate studies.

References:

-Asanuma H, Tamakwa K, Niitsuma H, Baria R, Häring M., 2011. Reflection Imaging of EGS Reservoirs at Soultz and Basel using Microseismic Multiplets as a Source. *Trans. GRC, 35:295-299.*

-Baker T, Granat R, Clayton R. W., 2005. Real-Time Earthquake Location Using Kirchhoff Reconstruction. *Bull Seism Soc Am.,* 95:699-707.

-Brinker P., 2003. Zur Entwicklung der Seismische Überwachung im Sanierungsbetrieb Aue. – WISMUT GmbH, Servicecenter Markscheidewesen.

-Buske S., 1999. Three-dimensional pre-stack Kirchhoff migration of deep seismic reflection data. *Geophysical J. Intern., 137:243–260.*

-Buske S., Gutjahr S., Sik S., 2009. Fresnel Volume Migration of single-component seismic data, *Geophysics, 74-6:WCA47-WCA55.*

-Červený V., Popov M. M., Pšenčík I., 1982. computation of wavefields in inhomogeneous media – Gaussian beam approach. *Geophys. J. Roy. Astr. Soc., 70:109-128.*

-Červený V., Klimes L., Pšenčík I., 1984. Paraxial ray approximation in the computation of seismic wavefields in inhomogeneous media. *Geophys. J. Roy. Astr. Soc., 79:89-104.*

-Claerbout J. F., 1968. Synthesis of a layered medium from its acoustic transmission response. *Geophysics, 33:264-269.*

-Daneshvar M. R., Clay S. C., Savage M. K., 1995. Passive Seismic imaging using microearthquakes. *Geophysics, 60-4:1178-1186.*

-Fernandez, L. M., van der Heever, P. K., 1984. Ground movement and damage accompanying a large seismic event in the Klerksdorp district. In: *Rockbursts and Seismicity in Mines* (N. C. Gay and Å. H. Wainwright, eds.), Symp. Ser. No. 6, pp. 193-198, S. Afr. Inst. Min. Metal., Johannesburg.

-Geiger L., 1910. Herdbestimmung bei Erdbeben aus den Ankunftzeiten. *Nachrichten von der Gesellschaft der Wissenschaften zu Göttingen, Mathematisch-Physikalische Klasse,* 331-349.

-Gibowicz S. J., 1979. Space and time variations of the frequency-magnitude relation for mining tremors in the Szombierki coal mine in Upper Silesia, Poland. *Acta Geophys. Pol., 27:39-49.*

-Gibowicz SJ, Kijko A. *An Introduction to Mining Seismology*. San Diego, USA: Academic Press, 1994.

-Grigoli F., Cesca S., Amoroso O., Emolo A., Zollo A., Dahm T., 2014. Automated seismic event location by waveform coherence analysis. *Geophys. J. Int., 196:1742-1753.*

-Grünthal G. *Erdbebenkatalog des Teritoriums der Deutschen Demokratischen Republik und angrenzend Gebiet von 823 bis 1984*. Potsdam, East Germany: Veröffentlichungen des Zentralinstituts für Physik der Erde, 1988.

-Gupta, H. A review of recent studies of triggered earthquakes by artificial water reservoirs with special emphasis on earthquakes in Koyna, India, *Earth Sci. 2002;58:279–310.*

-Häring O., Schanz U., Lnder F., Dyer B C., 2008. Characterisation of Basel 1 enhanced geothermal system. *Geothermics, 37:469-495.*

-Hassani H., Hloušek F., Alexandrakis C., Buske S., 2018. Migration-based microseismic event location in the Schlema-Alberoda mining area. *International Journal of Rock Mechanics and Mining Sciences, 110:161-167.*

-Hiller A., Schuppan W. *Geologie und Uranbergbau im Revier Schlema-Alberoda.* Dresden, Germany: Sächsische Landesamt für Umwelt und Geologie (LfUG); 2008.

-Hloušek F., Hellwig O., Buske S., 2015. Three-dimensional focused seismic imaging for geothermal exploration in crystalline rock near Schneeberg, Germany. *Geophysical Prospecting, 63:999–1014.*

- Kao H., Shan S. J., 2004. The Source-Scanning Algorithm, mapping the distribution of seismic sources in time and space. *Geophys. J. Int., 157:589-594.*

-Korobko V. G., Grebenkin V. F. *Durchführung geothermischer Untersuchungen und Temperaturbeobachtungen in den Schächten des Objektes 09. - SDAG Wismut, Objekt 36, Grüna. Wismut GmbH, Unternehmensarchiv; Sign. WTZ- 3008, 1960.*

-Knoll P., 1990. The fluid-induced tectonic rockburst of March 13, 1989 in the "Werra" potash mining district of the GDR (first results). *Beitr. Geophys., 99:239-245.*

-Künzel U. *Seismizität im Umfeld der Uranerzlagerstätte Schlema-Alberoda und modifizierte Auswertemethoden für eine präzise Lage- und Stärkeermitlung der im Nahfeld instrumentell registerierten Mikrobeben*. Freiberg, Germany: Veröffentlichungen des Instituts für Geotechnik der Technischen Universität Bergakademie Freiberg; 2013.

-Leydecker G. *Erdbebenkatalog für die Bundesrepublik Deutschland mit Randgebieten für die Jahre 800 bis 2008.* Hannover, Germany: Bundesanstalt für Geowissenschaften und Rohstoffe (BGR); 2011.

-McGarr A., Simpson D. In: Rockbursts and seismicity in mines. Balkema, pp385-396, 1997.

-McGarr A, Simpson D., Seeber L. *Case histories of induced and triggered seismicity*. In: Lee WHK, .Kanamori H, Jennings PC, Kisslinger C, eds. San Francisco: Academic Press; International Handbook of Earthquake and Engineering Seismology; 81A, 647–661, 2002.

-McMechan G.A., Luetgert J.H., Mooney W.D., 1985. Imaging of earthquake sources in Long Valley Caldera, California, 1983. *Bull Seism Soc Am.,* 75:1005-1020.

-Neidel N.S., Taner T., 1971. Semblance and other coherency measures for multichanel data. *Geophysics, 36-3:482-497.*

-Officer C. B., *Introduction to the theory of sound transmission*. McGraw-Hill Book Co., 1958.

-Oye V., Roth M., 2003. Automated seismic event location for hydrocarbon reservoirs. *Computers & Geosciences,* 29:851-863.

-Petschat U. *Geomechanische Forschungen und Ergebnisse in den Lagerstätten des Bergbaubetriebes 9 Aue.* SDAG Wismut, BB Aue; WISMUT GmbH, Geolog. Archiv, 1986: Inv.-Nr. A-167.

-Penzel M., Wallner O., 2004. Die Verfahrung des Komplexen Bruchgebietes Oberschlema als Voraussetzung für die Entstehung eines Kurparks. *4. Altbergbaukolloquium Mintanuniversität Leoben, Tagungsband; S.257-269.*

-Podvin P., Lecomte I., 1991. Finite difference computation of traveltimes in very contrasted velocity models: a massively parallel approach and its associated tools. *Geophysical Journal International, 105: 271–284.*

-Rentsch S., Buske S., Gutjahr S., Kummerow J., Shapiro S.A., 2010. Migration-based location of seismicity recorded with an array installed in the main hole of San-Andreas Fault Observatory at Depth (SAFOD). *Geophys. J. Int., 182:477-492.*

-Reshetnikov A., Buske S., Shapiro S.A., 2010. Seismic imaging using microseismic events: Results from the San Andreas Fault System at SAFOD. *J. Geophys. R., 115:B12324.*

-Roberts R. G., Christoffersson A., Cassidy F., 1989. Real time event detection, phase identification and source location using single station three components seismic data. *Geophys. J. Roy. Astr. Soc., 97:471480.*

-Schneider W.A., 1978. Integral formulation for migration in two and three dimensions. *Geophysics., 43:49–76.*

-Shapiro S.A. *Microseismicity, a tool for reservoir characterization*. Houten, Netherlands: EAGA Publications bv; 2008.

-Soma N., Niitsuma H., Baria R., 2002. Evaluation of Subsurface Structures at Soultz Hot Dry Rock Site by the AE Reflection Method in Time-frequency Domain. *Pure appl. geophys., 159:543-562.*

-Trojanowski J., Eisner L., 2016. Comparison of migration-based location and detection methods for microseismic events. *Geophysical Prospecting, 65-1:47-63.*

-Vidale J.E., 1988. Finite-difference calculation of travel times. *Bull. Seismol. Soc. Am., 78;2062-76.*

-Vinje V., Iversen E., Gjoysdal H., 1993. Traveltime and amplitude estimation using wavefront construction. *Geophysics, 58:1157-1166.*

-Wadati K., 1933. On the travel time of earthquake waves, part II. *Geophys. Mag.,* 7:101-11.

-Wallner O., Hiller A., Frenzel M., Frommhold R. *Detailierte geowissenschaftliche Datenaufbereitung im Vorzugsgebiet Aue-Schwarzenberg im Rahmen des Tiefengeothermieprojektes Sachsen (Internal Report).* Wismut GmbH; 2009.

-Wallner O. *Analyse bergbauinduzierter Bodenbewegungen und Seismizität während der Gewinungs- und Flutungsphase einer komplexen Gangerzlagerstätte.* Dissertation: TU Bergakademie Freiberg; 2009.

-Yilmaz Ö. *Seismic data analysis: Processing, Inversion and Interpretation of Seismic Data.* Vol. 1, Society of Exploration Geophysics, 2001.

Appendix:

Located events in the Schlema-Alberoda. The coordinates are in a local Cartesian coordinate system. The timestep refers to the iterative migration (see section A-6-4).

yy.mm.dd	x	y	z	Origin time	timestep
98.03.02	8150	6550	1575	13:03:34,81	68
98.05.10	8475	6400	1575	12:27:57,63	75
98.05.29	8550	6800	1075	13:44:47,28	50
99.01.02	8350	6775	1375	17:01:31,82	67
99.01.11	8325	6750	1350	02:47:07,38	65
99.02.01	9300	5525	1225	00:52:24,87	83
99.03.19	8525	6475	1550	14:42:06,13	94
99.04.26	8250	6800	1325	12:21:46,50	64
99.05.11	7850	6375	1725	05:31:32,73	61
99.07.09	7925	7550	850	15:01:00,82	62
99.08.01	7850	6550	1475	00:46:23,72	96
00.06.21	8200	6550	1175	10:13:37,19	61
01.05.23	8475	6575	875	16:40:03,46	52
01.11.16	8000	7100	250	08:24:12,29	29
03.03.12	8025	7650	550	15:20:10,98	22
03.11.27	8675	6225	1325	14:40:40,96	75
03.11.28	8825	6125	1350	01:17:40,57	83
06.01.07	8175	7325	1225	15:25:12,59	51
06.01.30	8325	7500	675	05:25:45,45	30
06.02.23	8125	6425	1850	16:04:15,38	72
06.02.25	7725	7525	750	14:03:23,48	25
06.02.26	8400	6675	1400	09:19:11,32	68
06.02.28	6875	7475	1375	05:43:20,70	57

06.03.01	8325	6350	1950	15:28:31,88	80
06.03.03	8475	6500	1550	16:28:17,98	76
06.03.20	8475	6575	1900	12:40:26,39	88
06.04.01	7950	7075	1100	08:13:27,95	49
06.04.01	7950	7100	1125	23:16:43,13	49
06.04.02	7825	7100	1025	04:31:51,32	45
06.04.12	8875	6275	1250	15:49:20,30	75
06.04.12	8900	6275	1325	16:17:37,70	77
06.04.13	9050	6075	1050	08:42:55,71	73
06.06.09	8550	6875	1325	19:59:10,44	69
06.06.10	8625	6525	1525	09:14:17,26	81
06.06.12	8650	6500	1525	22:59:21,54	82
06.06.29	8825	6225	1225	08:33:13,31	74
06.06.29	8825	6225	1225	12:34:32,29	74
06.07.24	8350	6575	1425	17:24:04,53	68
06.08.05	8825	6125	1450	07:51:14,97	79
06.08.12	8275	6700	1550	20:08:23,48	74
06.08.27	8625	5625	825	17:11:21,39	57
06.09.21	8475	6450	1350	05:03:18,39	71
06.10.06	8875	5475	1000	03:33:41,45	70
06.10.30	7800	6400	1925	01:03:23,97	88
06.11.09	7600	6900	1875	18:26:12,88	86
06.11.26	7700	6725	2025	17:28:13,84	85
07.01.14	9200	5950	1625	18:35:57,11	98
07.02.06	7975	7050	1075	17:57:16,28	50
07.02.06	7975	7025	1050	17:57:38,23	51
07.02.07	8125	7275	900	14:01:35,45	61
07.02.10	8300	7250	1075	13:45:56,72	52
07.03.26	7825	7200	1075	02:48:26,99	73
07.04.01	7950	7650	800	11:54:24,53	24
07.04.19	9025	5950	850	18:46:07,16	63
07.07.27	7625	6925	1300	22:40:47,30	57

07.08.03	7575	6550	1250	19:00:59,10	46
07.08.04	8775	6250	475	18:37:16,07	48
07.09.25	8100	8475	325	02:21:06,69	36
07.10.13	7875	7775	1075	06:28:05,54	31
07.10.13	9000	5900	725	12:38:26,85	57
07.10.16	8950	6075	925	04:36:34,80	66
07.11.04	7825	6750	1375	16:15:40,76	60
07.11.17	7675	7200	1400	08:31:55,83	57
07.11.18	7925	7025	1800	17:51:02,83	79
07.11.18	8000	7025	1100	17:51:12,40	52
07.11.18	8300	7050	1425	18:11:05,92	69
07.12.18	7975	7075	1000	21:48:32,79	54
07.12.25	7750	7100	1025	09:51:32,12	44
07.12.26	8175	6450	2025	08:14:10,55	108
08.01.03	7825	7300	1375	19:36:27,27	58
08.01.05	7800	7675	1000	13:11:06,87	26
08.01.10	9875	7850	1475	04:29:58,85	98
08.01.10	9375	7750	1325	04:38:31,09	81
08.01.12	8700	6400	1525	04:28:58,93	89
08.01.15	8275	7275	1000	18:50:29,78	45
08.01.16	9850	5275	1625	09:30:40,22	112
08.01.16	8950	6175	3225	20:21:49,49	156
08.01.22	8925	6150	1450	00:55:37,27	79
08.01.22	8950	6100	1375	08:04:06,22	77
08.02.18	7975	7575	800	11:38:58,52	23
08.02.19	7925	7625	700	01:28:12,47	21
08.02.21	9225	5875	1275	18:46:24,60	83
08.03.02	9000	6000	1000	07:46:44,27	70
08.03.10	7725	7525	1100	23:21:57,47	34
08.04.13	8175	7175	925	04:18:57,76	47
08.04.14	7725	6800	775	03:25:54,29	53
08.04.20	7875	6800	1300	01:20:32,87	64

08.04.23	8925	6300	1650	22:17:41,65	103
08.04.24	7725	6675	1425	00:19:42,82	70
08.05.09	7875	6950	1125	16:01:27,43	82
08.05.24	9250	5775	1200	19:48:09,19	80
08.05.25	8075	7125	1225	12:01:58,61	53
08.05.27	7950	6825	1350	18:18:21,46	65
08.06.06	8100	6275	1550	04:09:11,46	91
08.06.11	9075	5800	2100	17:13:22,06	112
08.06.16	7950	7400	1100	10:06:09,26	46
08.07.01	9250	5300	1250	02:57:34,45	87
08.08.16	8350	6475	1475	08:33:47,84	86
08.08.31	8650	6525	1500	04:14:13,58	89
08.09.14	8875	5550	1025	14:06:49,85	70
08.09.15	7775	6750	1550	16:21:00,47	71
08.10.19	7425	7675	1950	09:12:10,97	69
08.10.27	9225	5850	1325	11:55:38,83	85
08.11.11	7925	6900	1375	21:20:57,57	62
08.11.22	9375	5900	1575	13:04:00,95	96
08.11.26	8975	6275	900	18:29:21,36	67
09.02.09	9250	6050	1800	08:52:28,88	109
09.02.22	8050	6975	1150	00:14:21,59	56
09.03.19	9050	5450	1725	21:57:06,27	105
09.04.11	9475	5875	1750	18:57:15,27	105
09.04.28	7900	7675	800	16:51:35,37	22
09.05.14	8075	7125	1125	05:40:37,99	51
09.05.16	7950	7150	1325	19:43:38,58	55
09.05.28	7975	6675	1600	08:56:24,36	77
09.10.25	8300	6250	2200	03:16:12,44	122
09.11.04	9050	6075	1125	20:14:51,36	76
09.11.04	8050	6275	1700	21:47:55,49	94
09.11.10	8050	6300	1700	06:03:11,33	93
09.11.21	8875	6300	900	07:15:04,72	68

10.01.06	8775	5975	1300	14:02:25,27	85
10.02.03	9250	5725	1800	05:41:09,18	106
10.04.16	7850	6800	1750	23:44:53,89	80
10.04.19	9225	5800	1275	19:16:22,32	83
10.05.11	8125	7125	1325	14:30:55,02	57
10.05.11	8125	7125	1275	16:52:04,69	56
10.09.16	9100	5850	875	15:14:22,91	64
10.10.22	8000	7050	1175	08:39:31,58	79
12.11.06	7950	6800	1250	15:04:57,62	75
12.01.24	3775	3150	2050	17:13:01,70	53
12.01.25	3825	3175	1825	05:16:36,08	67
12.01.25	3825	3400	1650	05:51:41,11	40
12.01.25	3750	3125	2150	06:04:34,75	71
12.01.25	3725	3150	2175	06:11:44,87	59
12.01.25	3875	3400	1700	06:21:38,64	84
12.01.25	3775	3175	2025	07:20:54,30	77